Interior structure of terrestrial planets: Modeling Mars' mantle andits electromagnetic, geodetic, and seismic properties

Olivier Verhoeven, A. Rivoldini, P. Vacher, A. Mocquet, Gael Choblet, Michel Menvielle, V. Dehant, T. van Hoolst, J. Sleewaegen, J.-P. Barriot, et al.

▶ **To cite this version:**

Olivier Verhoeven, A. Rivoldini, P. Vacher, A. Mocquet, Gael Choblet, et al.. Interior structure of terrestrial planets: Modeling Mars' mantle andits electromagnetic, geodetic, and seismic properties. Journal of Geophysical Research. Planets, 2005, 110 (E4), pp.E04009. ⟨10.1029/2004JE002271⟩. ⟨hal-00155776⟩

HAL Id: hal-00155776

https://hal.science/hal-00155776v1

Submitted on 26 Jan 2016

HAL is a multi-disciplinary open access archive for the deposit and dissemination of scientific research documents, whether they are published or not. The documents may come from teaching and research institutions in France or abroad, or from public or private research centers.

L'archive ouverte pluridisciplinaire **HAL**, est destinée au dépôt et à la diffusion de documents scientifiques de niveau recherche, publiés ou non, émanant des établissements d'enseignement et de recherche français ou étrangers, des laboratoires publics ou privés.

HAL Authorization

Interior structure of terrestrial planets: Modeling Mars' mantle and its electromagnetic, geodetic, and seismic properties

O. Verhoeven,[1,2] A. Rivoldini,[1] P. Vacher,[2] A. Mocquet,[2] G. Choblet,[2] M. Menvielle,[3,4] V. Dehant,[1] T. Van Hoolst,[1] J. Sleewaegen,[1] J.-P. Barriot,[5] and P. Lognonné[6]

Received 26 March 2004; revised 7 February 2005; accepted 15 February 2005; published 13 April 2005.

[1] We present a new procedure to describe the one-dimensional thermodynamical state and mineralogy of any Earth-like planetary mantle, with Mars as an example. The model parameters are directly related to expected results from a geophysical network mission, in this case electromagnetic, geodetic, and seismological processed observations supplemented with laboratory measurements. We describe the internal structure of the planet in terms of a one-dimensional model depending on a set of eight parameters: for the crust, the thickness and the mean density, for the mantle, the bulk volume fraction of iron, the olivine volume fraction, the pressure gradient, and the temperature profile, and for the core, its mass and radius. Currently, available geophysical and geochemical knowledge constrains the range of the parameter values. In the present paper, we develop the forward problem and present the governing equations from which synthetic data are computed using a set of parameter values. Among all Martian models fitting the currently available knowledge, we select eight candidate models for which we compute synthetic network science data sets. The synergy between the three geophysical experiments of electromagnetic sounding, geodesy, and seismology is emphasized. The stochastic inversion of the synthetic data sets will be presented in a companion paper.

Citation: Verhoeven, O., et al. (2005), Interior structure of terrestrial planets: Modeling Mars' mantle and its electromagnetic, geodetic, and seismic properties, *J. Geophys. Res.*, *110*, E04009, doi:10.1029/2004JE002271.

1. Introduction

[2] The thermodynamical and mineralogical characterization of telluric planetary interiors requires the use of astronomical, geophysical, geological, and geochemical data, together with inputs from laboratory experiments. The preparation of future missions dedicated to in situ planetary exploration, offers the opportunity of building up research strategies, which incorporate various types of data in a single inversion for planetary structure. We believe that such planetological methods can also be valuable for the inversion of the huge data set already available for the Earth. Here, we describe a synergism between geophysical groups, which worked together for the preparation of the NetLander mission to Mars [*Harri et al.*, 1999].

[3] The objective of a Mars Network Science (MNS) mission is to deploy a network of identical landers on the Martian surface. Among other instruments, a magnetometer, a spatial geodesy experiment, and a seismometer are particularly relevant for the study of the deep interior of a planet. They were already part of the NetLander scientific payload (magnetometer (MagNet) [*Menvielle et al.*, 2000], geodesy experiment (NEIGE) [*Barriot et al.*, 2001], and seismometer (SEIS) [*Lognonné et al.*, 2000]).

[4] The goal of a MNS package is to provide enough constraints on the structure of Mars' interior, so that no a priori assumption regarding the thermal state and a minimal set of assumptions regarding the mineralogical composition of the mantle are required. This paper and its companion devoted to the inversion of MNS data can be regarded as the first steps toward this ambitious goal. In order to restrict as much as possible the number of assumptions required by the joint interpretation of the geophysical data sets, we summarize the internal structure of the planet as a one-dimensional model described by a restricted set of parameters: for the crust, the thickness and the mean density, for the mantle, the bulk volume fraction of iron, the olivine volume fraction, the pressure gradient and the temperature profile, and for the core, its mass and radius. The originality of the approach comes from the diversity of the processed geophysical data sets, which are related to the parameters by different kinds of equations: equations derived from a potential for the geodetic data, diffusion equations for the electromagnetic data, propagation equations for the seismic waves, and constitutive and PVT (Pressure-Volume-Temperature) equations for the physical properties of mantle minerals.

[1]Royal Observatory of Belgium, Brussels, Belgium.
[2]Laboratoire de Planétologie et Géodynamique, UMR-CNRS 6112, Université de Nantes, Nantes, France.
[3]CETP/IPSL, UMR CNRS/UBSQ 8639, Observatoire de Saint-Maur, Saint Maur des Fossés, France.
[4]Université Paris-Sud, Paris, France.
[5]Groupement de Recherche en Géodésie Spatiale, CNES, Toulouse, France.
[6]Département de Géophysique Spatiale et Planétaire, UMR7096, Institut de Physique du Globe de Paris, Saint Maur des Fossés, France.

Copyright 2005 by the American Geophysical Union.
0148-0227/05/2004JE002271

[5] In the present paper (1) we describe the forward problem, defined by the resulting system of nonlinear equations, (2) we construct a set of eight candidate models of the Martian mantle, and (3) we compute the synthetic geophysical profiles (i.e., output of the forward problem corresponding to MNS processed observations) corresponding to each of them, and finally (4) we discuss the relevancy of the candidate models. Whenever necessary we use available results from Earth studies, space missions, and laboratory experiments. The forward problem must be stated as completely as possible, in order to restrict the number of possible models during the subsequent inversion. It must also be expressed in a way as simple as possible, because it will have to be evaluated many times during the later inversion process, which will be of stochastic nature due to the nonlinear character of the problem. We pay a particular attention to the choices of the hypotheses used, of the model definition, of the thermodynamical concepts, and of the uncertainties on the data. These choices define the limit of validity of the results.

[6] The mathematical background, the algorithm of the inverse method, and the discussion of the inversion results are detailed in a companion paper (A. Rivoldini et al., manuscript in preparation, 2005).

[7] After briefly reviewing, in section 2, the current uncertainties regarding the structure and the mineralogical composition of the Martian mantle, the MNS geophysical data, the parameters governing the internal structure and the relevant equations are described in section 3. The link between the MNS data, the fundamental thermodynamical parameters and the laboratory data set are also addressed in this section. The scheme of the forward problem is presented in section 4. We choose eight sets of parameter values, thus defining the candidate models. These models are constructed in such a way that they are consistent with the current knowledge on Mars' interior. The description of these eight models, and the discussion of their corresponding geophysical data are presented in section 5. Appendix A is devoted to the complete description of the method used in the forward problem to compute the density and bulk modulus of any mineral at a given pressure and temperature.

2. Current Uncertainties Regarding the Structure and Mineralogy of the Martian Mantle

[8] At the moment, the modeling of Mars' internal structure is only constrained by a small number of geophysical observations: mass, size, surface pressure and temperature [e.g., *Born*, 1974; *Bills and Ferrari*, 1978], precession rate, variation in rotation rate [*Folkner et al.*, 1997; *Yoder and Standish*, 1997; *Yoder et al.*, 2003], magnetic and gravity fields [e.g., *Acuña et al.*, 1999; *Lemoine et al.*, 2001; *Langlais et al.*, 2004], and tidal constraints [e.g., *Lognonné and Mosser*, 1993; *Yoder et al.*, 2003]. These insights were mainly obtained from orbital space missions [e.g., *Gapcynski et al.*, 1977; *Zuber et al.*, 2000], and from Earth-bound monitoring data (for a review, see *Kieffer et al.* [1992] and *Spohn et al.* [1998]).

[9] There is still not enough data to resolve, for example, the ambiguities regarding the size and state of the core, the possible presence of a solid inner core and the thermal and mineralogical composition of the mantle. The present knowledge of the Martian crust is also very poor and large uncertainties remain in the mean density of the crust, in the presence of a light primary crust [*Wieczorek and Zuber*, 2004] and on the density differences between the crust and the Martian volcanoes. Beside the astronomical and geophysical observations, constraints on the Martian chemical composition can be inferred from laboratory analysis of SNC (Shergottites, Nakhlites, Chassigny) meteorites, which are usually assumed to be of Martian origin [e.g., *Dreibus and Wänke*, 1985; *McSween*, 1985]. Present models of the Martian internal structure rely therefore on additional hypotheses. This is illustrated by Model A of *Sohl and Spohn* [1997] based on geophysics, the model of *Bertka and Fei* [1998] based on laboratory experiments, and that of *Sanloup et al.* [1999], based on geochemical modeling. Model A of *Sohl and Spohn* [1997] was derived from a SNC chemical composition, and it was designed to satisfy the value 0.366 of the moment-of-inertia factor. Taking into account the SNC geochemical constraints, the model of *Bertka and Fei* [1998] focused on the computation of the density profile of the mantle. The model was designed to satisfy the mass and the moment-of-inertia factor of the planet. *Sanloup et al.* [1999], on the other hand, relaxed the SNC hypothesis and considered the Martian composition as a mixture of H ordinary chondrites, and EH enstatite chondrites. One of the two particular mixtures they considered satisfies the constraints imposed by the measured data, except for a smaller value of the polar moment of inertia. The *Sohl and Spohn* [1997] and *Bertka and Fei* [1998] models were constructed to fit a moment-of-inertia factor close to the value of 0.3650 ± 0.0012 obtained by *Yoder et al.* [2003].

[10] The bulk chemical composition of any Martian model based on SNC geochemical constraints, is different from the CI chondritic composition of the protoplanetary nebula [*Longhi et al.*, 1992] if the crust is thinner than 100 km [*Bertka and Fei*, 1998]. In fact, the set of currently available data is still not sufficient to derive a unique model of Martian mineralogy without any a priori assumption. For example, values of the core radius and core density in the ranges 1500–2000 km, and 6.0–7.5 g/cm^3, respectively, can explain equivalently the values of total mass and moment of inertia, depending on the temperature and iron content of the mantle, and on the globally averaged thickness of the Martian crust [*Mocquet et al.*, 1996; *Yoder and Standish*, 1997].

3. Data, Parameters, and Constitutive Relationships

[11] In what follows, we call "data" geophysical quantities which are independently processed from each experiment. Those are (1) the total mass of Mars M, (2) the mean moment of inertia of the crust and the mantle $I_{m,c}$ in spherical geometry, (3) the value of the electrical conductivity $\sigma(r)$ at radius r, and (4) the acoustic wave speed $v_\phi(r)$ at radius r.

[12] We call "parameters" the eight quantities that govern our modeling of the internal structure of Mars: (1) the crustal thickness h_{crust}, (2) the mean density of the crust ρ_{crust}, (3) the bulk fraction of iron in the mantle x_{Fe}, (4) the olivine volume fraction of the mantle X_{ol}, (5) the pressure gradient in the mantle dP/dr, (6) the temperature profile of

Table 1. A Priori Knowledge: Constants Needed for the Computation of the Electrical Conductivity as a Function of Temperature and Iron Content[a]

Mineral Name	Formula	$\log \sigma_{0;\,ref}^{(i)}$	$E_{0;\,ref}^{(i)}$, eV	$\alpha^{(i)}$	$\beta^{(i)}$, eV
1- olivine	$(Mg_{1-y}\,Fe_y)_2SiO_4$	2.69[b,c]	1.62[b,c]	2.42[c]	−0.485[c]
2- wadsleyite	$(Mg_{1-y}\,Fe_y)_2SiO_4$	3.29[b]	1.29[b]	2.42[d]	−0.485[d]
3- ringwoodite	$(Mg_{1-y}\,Fe_y)_2SiO_4$	2.92[b]	1.16[b]	2.42[d]	−0.485[d]
4- Mg-perovskite	$(Mg_{1-y}\,Fe_y)SiO_3$	1.28[b,e]	0.61[b,e,f,g]	3.56[e]	−1.72[e]
5- Mg-wüstite	$(Mg_{1-y}\,Fe_y)O$	2.56[b,h]	0.81[b,f,h]	3.14[h]	0.[h]
6- clinopyroxene LP	$(Mg_{1-y}\,Fe_y)SiO_3$	3.19[b]	1.86[b]	−1.28[i]	−1.41[i]
7- clinopyroxene HP	$(Mg_{1-y}\,Fe_y)SiO_3$	3.19[j]	1.86[j]	−1.28[j]	−1.41[j]
8- orthopyroxene	$(Mg_{1-y}\,Fe_y)SiO_3$	3.66[b,k]	1.79[b,k]	−1.28[k]	−1.41[k]
9- Ca-pyroxene	$Ca\,(Mg_{1-y}\,Fe_y)Si_2O_6$	3.19[j]	1.86[j]	−1.28[j]	−1.41[j]
10- akimotoite	$(Mg_{1-y}\,Fe_y)SiO_3$	3.29[b,l]	1.65[b,l]	−1.28[i]	−1.41[i]
11- majorite	$(Mg_{1-y}\,Fe_y)SiO_3$	3.29[b,l]	1.65[b,l]	−1.28[i]	−1.41[i]

[a]See equations (13) and (14). For each mineral i, $\sigma_{0;\,ref}^{(i)}$ and $E_{0;\,ref}^{(i)}$ represent the preexponential factor and the activation energy, respectively, for an iron fraction y equal to 0.1 (i.e., Mg# = 0.9). The constants $\alpha^{(i)}$ and $\beta^{(i)}$ govern the iron content contribution to the preexponential factor and the activation energy, respectively. The details of the computation of this table are given by P. Vacher and O. Verhoeven (submitted manuscript, 2004), except for Ca-pyroxene, whose electromagnetic constants are assumed identical to low-pressure (LP) clinopyroxene values.
[b]*Xu et al.* [2000].
[c]*Hinze et al.* [1981].
[d]α and β identical to olivine values.
[e]α and β identical to pv/mw assemblage values computed from *Poirier and Peyronneau* [1992].
[f]For the minerals of the lower mantle, Mg-perovskite and Mg-wüstite, an activation enthalpy computed at 25 GPa is given instead of the activation energy to account for high pressure effect.
[g]*Shankland et al.* [1993].
[h]*Dobson and Brodholdt* [2000].
[i]α and β identical to orthopyroxene values.
[j]log σ_0, E_0, α and β identical to clinopyroxene LP values.
[k]*Seifert et al.* [1982].
[l]Values computed from log σ_0, E_0 values reported by *Xu et al.* [2000] for ak + gt.

the mantle $T(r)$, (7) the radius of the core r_{CMB}, and (8) the core mass M_C.

[13] The currently a priori knowledge consists of constitutive equations and equations of state (hereafter called PVT equations) and of physical constants. The values of those constants are obtained from laboratory results and summarized in Tables 1 and 2. The constitutive relationships are derived from theoretical considerations, empirical relations and laboratory experiments.

3.1. Modeling Hypotheses

[14] A fundamental hypothesis of the present work is that a future network science mission on Mars is expected to provide data representative of the whole planet, regardless of the extension of the network. It is thus assumed that the sampling of the deep planet is sufficiently homogeneous, and that the effects of lateral heterogeneities are smoothed out along seismic ray paths. Possible deviations from one-dimensional structure are expected to be mainly related to the Tharsis rise and to the dichotomy, but they are disregarded in this study. In the following, we thus consider a spherically symmetric, in hydrostatic equilibrium, and isotropic model of internal structure, which is described by a minimal set of parameters. Three main chemically homogeneous regions are considered: the crust, the mantle (with possible phase transitions), and the core. In the present paper, our modeling focuses on the details of mantle structure, with the crust and the core described by integrated parameters.

3.2. MNS Data Sets

[15] In this section, we describe the main equations used to obtain MNS data from the measurements performed by the experiments on the Martian surface. The uncertainties associated with these processed data are also discussed. These uncertainty values will constrain the possible values of the parameters during the future inversion of the MNS data sets (to be published elsewhere). The rest of the paper is devoted to a comprehensive description of the forward problem, which links the parameters describing the internal structure of Mars to the processed MNS data sets.

3.2.1. Network Geodesy Experiment

[16] The geodesy experiment NEIGE (NEtlander Ionosphere and Geodesy Experiment) is based on the observation of a radio-signal between the landers and an orbiter around Mars, and between this orbiter and the Earth [*Barriot et al.*, 2001]. The Doppler effect on these signals is related to the relative velocities involved in the radio-links. By using the Doppler shift measurements, it is possible to obtain the positions and the orientation of Mars in space, as well as their variations. It must be noted that the signal between the landers and the orbiter crosses the ionosphere which perturbs the signal. The use of two different frequencies allows to correct for this effect and to characterize the ionosphere. The NEIGE experiment has thus two different aspects, one related to geodesy, and the other related to the ionosphere. The geodesy part of NEIGE aims at obtaining Mars' rotation (variations of the length of day), its precession and nutations (motion of the rotation axis in space), and its polar motion (motion of the rotation axis in a frame tied to the planet), and at deriving properties of Mars' interior from these observations. The coefficients of a spherical harmonic description of the gravity field are obtained from the orbiter position and velocity perturbations. The degree zero coefficient is equal to GM, where G is the universal gravitational constant, and M the total mass

Table 2. A Priori Knowledge: Laboratory Results Concerning Elastic Properties of Minerals i[a]

Mineral Name	$\rho_0^{(i)}$, 10^3 kg m^{-3}	$\rho_{0,Fe}^{(i)}$, 10^3 kg m^{-3}	$a_0^{(i)}$, K^{-1}	$b_0^{(i)}$, K^{-2}	$c_0^{(i)}$, K	$\gamma_{th_0}^{(i)}$	$K_{S_0}^{(i)}$, GPa	$K_{S_0Fe}^{(i)}$, GPa	$\left.\frac{\partial K_S^{(i)}}{\partial P}\right\|_0$	$\left.\frac{\partial K_S^{(i)}}{\partial T}\right\|_0$, GPa K^{-1}
1- olivine	3.222	1.182	2.832	0.758	0.	1.14	129.[b]	0.	4.2[b]	−0.016[b]
2- wadsleyite	3.472	1.24	2.711	0.6885	0.5767	1.32	172.[c]	0.	4.5[c]	−0.016[d]
3- ringwoodite	3.548	1.30	1.872	0.421	0.6537	1.21	185.[e]	35.[e]	4.1[e]	−0.024[f]
4- Mg-perovskite	4.108	1.07	1.17[g]	1.51[g]	0.	1.31	264.	0.	4.0	−0.015
5- Mg-wüstite	3.584	2.28	3.0[h]	1.2[h]	0.	1.45[h]	163.	−15.[i]	4.0[j]	−0.019
6- clinopyroxene LP	3.208[k]	0.80[l]	2.86[m]	0.72[m]	0.	1.05[m]	112.[k]	−5.[m]	6.6[k]	−0.012[m]
7- clinopyroxene HP	3.297[k]	0.82[l]	2.86	0.72	0.	1.05	112.[k]	−5.[m]	6.6[k]	−0.012[m]
8- orthopyroxene	3.194[n]	0.81[l]	2.86	0.72	0.	1.05	109.[o]	−5.[n]	7.0[o]	−0.012[p]
9- Ca-pyroxene	3.277	0.38	2.32[q]	1.88[q]	0.	1.06	105.	13.	6.2-1.9x_{Fe}	−0.013
10- akimotoite	3.810	1.1	2.27	0.682	−0.385	1.38[r]	212.	0.	5.6	−0.017
11- majorite	3.565	0.76	2.08[s]	1.43[s]	0.	1.17[s]	171.	15.[t]	4.4	−0.021

[a]Unless stated otherwise, the data are taken from the compilation of *Vacher et al.* [1998] and the values of Grüneisen parameter $\gamma_{th_0}^{(i)}$ are taken from *Ita and Stixrude* [1992]. Other references are as listed. $\rho_0^{(i)}$ and $K_{S_0}^{(i)}$ refer to the density and the bulk modulus of the ith mineral at STP conditions (STP: $P_0 = 10^5$ Pa, $T_0 = 298$ K). $\left.\frac{\partial K_S^{(i)}}{\partial P}\right|_0$ and $\left.\frac{\partial K_S^{(i)}}{\partial T}\right|_0$ denote the derivatives, at STP conditions, of the bulk modulus of the ith mineral with respect to P and T, respectively. $\rho_{0,Fe}^{(i)}$ and $K_{S_0Fe}^{(i)}$ give the iron content dependence of the density and bulk modulus, respectively (see section 3.4.3). The coefficients $a_0^{(i)}$, $b_0^{(i)}$, and $c_0^{(i)}$ govern the thermal expansion (15). The constants $d_0^{(i)}$ in the thermal expansion (15) are equal to zero except for the akimotoite, for which it is equal to −0.1808. LP refers to low pressure; HP refers to high pressure.

[b]*Zha et al.* [1998].
[c]*Li and Liebermann* [2000].
[d]*Katsura et al.* [2001].
[e]*Sinogeikin et al.* [1998, 2001].
[f]*Jackson et al.* [2000].
[g]*Fiquet et al.* [1998].
[h]*Dewaele et al.* [2000].
[i]*Zhang and Kostak* [2002].
[j]*Sinogeikin and Bass* [2000].
[k]*Angel and Hugh-Jones* [1994].
[l]*Woodland and Angel* [1997].
[m]Same as orthopyroxene.
[n]*Jackson et al.* [1999].
[o]*Flesch et al.* [1998].
[p]*Duffy and Anderson* [1989].
[q]*Zhao et al.* [1998].
[r]*Reynard and Rubie* [1996].
[s]*Wang et al.* [1998].
[t]*Sinogeikin and Bass* [2002], *Wang and Ji* [2001], *Zhang et al.* [1999].

of the planet. The degree two coefficient A_{20} is related to the principal moments of inertia (A, B, and C) by

$$A_{20} = G\left(\frac{A+B}{2} - C\right) = G(\bar{A} - C), \tag{1}$$

where $\bar{A} = (A + B)/2$ is the mean equatorial moment of inertia. Using the precession rate, which is proportional to $\frac{C-\bar{A}}{C}$, we compute the mean moment of inertia $I = \frac{2\bar{A}+C}{3}$. The observation of the Chandler wobble, of which the frequency is also proportional to $\frac{C-\bar{A}}{C}$ can be used in addition to constrain the value of I.

[17] The NEIGE experiment is designed to improve by one order of magnitude the knowledge of the mean moment of inertia of Mars, reaching an uncertainty of 0.05%. The uncertainty on the mass of Mars is similar. On the other hand, the nutations that will be observed by NEIGE, are very much influenced by the physical state of the core: when the core is at least partially liquid, there is a resonance amplifying the amplitudes of the nutations, due to the existence of a rotational normal mode called the Free Core Nutation [*Dehant et al.*, 2000]. The observation of this resonance will allow us to deduce the physical state of the core, the core mean moment of inertia, and its dynamical flattening and thus to constrain its dimension. The strategy to derive these parameters is explained by *Yseboodt et al.* [2003]. The core mean moment of inertia I_C is expected to be obtained with an uncertainty of 20%. Therefore the uncertainty on the mean moment of inertia $I_{m,c}$ of the crust and the mantle is evaluated as

$$\frac{\Delta I_{m,c}}{I_{m,c}} = \frac{I}{I_{m,c}}\frac{\Delta I}{I} + \frac{I_C}{I_{m,c}}\frac{\Delta I_C}{I_C} \tag{2}$$

$$= \left(\frac{I_C}{I_{m,c}} + 1\right) 0.05\% + \frac{I_C}{I_{m,c}}\, 20\% \sim 1\% \tag{3}$$

for a fraction $\frac{I_C}{I_{m,c}}$ roughly equal to 5%, a fraction reasonable regarding the current models of the Martian interior [see, e.g., *Sohl and Spohn*, 1997].

3.2.2. Network Magnetometer Experiment

[18] The network magnetometer experiment is based upon the analysis of continuous recordings of the three components of the magnetic field at at least three network stations (see, e.g., *Menvielle et al.* [2000] for an extensive description of the network magnetometer experiment proposed for NetLander, MagNet).

[19] The study of the electrical structure of the planet is performed by means of electromagnetic sounding techniques, based upon the estimation and analysis of the complex inductive impedance, which characterizes the inductive response of the conductive planet. The inducing primary

field is the transient magnetic field of external origin, which is the magnetic signature of the plasma flow and current in the ionized environment; the secondary induced field of internal origin depends on time and space characteristics of the external field, and on the distribution of electrical resistivity inside the planet. Qualitative considerations suggest that the primary external field has an intensity of typically few 10 nT, with frequencies ranging from few Hz down to about 10^{-5} Hz, and even less, and spatial wave number from regional (few 10^{-6} m^{-1}) to planetary (few 10^{-8} m^{-1}) scales [see, e.g., *Menvielle et al.*, 1996, 2000].

[20] The Mars Global Surveyor magnetometer experiment [*Acuña et al.*, 1999] has demonstrated the existence of large magnetic anomalies, which are the signature of Mars crust remanent magnetization. Direct interaction between the interplanetary magnetic field (IMF) and these anomalies exists when the magnetic field of crustal origin is intense enough at the outer boundary of the Mars ionized environment to make possible its magnetic reconnection with the IMF. Such interaction, demonstrated on the Mars Global Surveyor magnetic observations [*Acuña et al.*, 1999], results in the formation of extended, multiple, Earth like magnetosphere cusps and magnetic reconnection regions. The spatial extent of these structures, and thus that of the associated external magnetic fields, is directly related to that of the responsible magnetic anomalies. We assume hereafter that the network configuration is consistent with the expected typical spatial wavelength of the external field far from the regions of intense static anomalies and that the landing sites of the network stations avoid these regions.

[21] In the case of the Earth, electromagnetic studies demonstrate that the electrical structure of the lithosphere and upper mantle can be described in terms of average 1-D models (where the conductivity σ only depends on the depth z) depending on the overall tectonic history of the region, with heterogeneous structures that mark present or past geodynamic structures [see, e.g., *Tarits and Jouanne*, 1990; *Hjelt and Korja*, 1993]. The present knowledge of Mars' inner structure strongly suggests that the same situation also prevails for its Northern lowlands and Southern highlands, separated by the dichotomy with the exception of large impact craters and volcanoes. We therefore assume that the Mars inner conductivity in the network area only depends on the depth (1-D situation), which comes down to the assumption that the network area does not encompass any major tectonic structure.

[22] The impedance Z can be related to the magnetic field $\mathbf{H}$ using Maxwell's equations [see, e.g., *Schmucker*, 1970; *Kuckes*, 1973a, 1973b; *Berdichevsky et al.*, 1976]:

$$Z(\omega) = -i\omega\mu \frac{H_z(\omega)}{\frac{\partial H_z(\omega)}{\partial z}} = i\omega\mu \frac{H_z(\omega)}{\frac{\partial H_x(\omega)}{\partial x} + \frac{\partial H_y(\omega)}{\partial y}}, \tag{4}$$

where ω is the frequency, x and y are in the horizontal plane, and z is the vertical direction; x, y, and z form a direct frame. μ is the magnetic permeability of the medium, equal to that of vacuum for most of geological materials on the Earth and therefore on Mars.

[23] Unfortunately, one cannot expect to directly obtain useful estimations of the horizontal gradients of the magnetic field from simultaneous measurements at only 3 different locations. We further assume that the field at the surface of Mars (and in the insulating Mars atmosphere) behaves as a superposition of independent plane waves $\mathbf{H}(\omega, \mathbf{k}(\omega))$ of wave vector $\mathbf{k}(\omega)$. In such a case the spatial gradient determination is equivalent to wave-vectors identification, which is performed using a multipoint data analysis technique initially developed in the frame of the ongoing ESA multispacecraft Cluster mission [*Pinçon and Lefeuvre*, 1991, 1992; *Motschmann et al.*, 1996]. This technique only allows us to estimate the modulus of the impedance $|Z(\omega, \mathbf{k}(\omega))|^2$, so that only apparent resistivities can be computed:

$$\rho_a(\omega, \mathbf{k}(\omega)) = \frac{1}{\omega\mu} |Z(\omega, \mathbf{k}(\omega))|^2 \tag{5}$$

(see *Pinçon et al.* [2000] for an extensive presentation of the technique analysis). The set of $\rho_a(\omega, \mathbf{k}(\omega))$ apparent resistivities computed using formula (5) with the estimated $\mathbf{k}(\omega)$ is then likely to be representative of the 1-D average structure of Mars below the network. We assume that the network area does not encompass any major tectonic structure.

[24] Finally, the conductivity profile $\sigma(r)$ and the corresponding confidence intervals are estimated from the variation with frequency of $\rho_a(\omega, \mathbf{k}(\omega))$ by means of 1-D inversion techniques already developed and used for the Earth. For further information on these techniques, the reader is referred to, e.g., *Parker and Whaler* [1981], to *Grandis et al.* [1999], and to *Parkinson and Hutton* [1989] for a review.

[25] The uncertainties on the computed conductivity profile $\sigma(r)$ result from (1) the noise on the magnetic measurements, (2) the effect of the network geometry on the wave field analysis, and (3) the impact of the uncertainties on the estimated $\rho_a(\omega, \mathbf{k}(\omega))$.

[26] Regarding the present state of the art for the flux-gate magnetometers, the noise on the magnetic measurements is mostly due to the magnetic field perturbations generated at the magnetometer sensor by the lander activities. Particular attention is paid to magnetic cleanliness issues during the lander design and test, to minimize as far as possible the intensity of this noise [*Kuhnke et al.*, 1998]. As a result of the a priori knowledge included during the wave field identification, the resulting effect is expected to be on the order of a few percent, or even less on individual $\mathbf{k}(\omega)$ determination.

[27] The horizontal gradient of the magnetic field is a two-dimensional structure; hence its determination requires, as a minimum, three stations in a two-dimensional configuration. The impact of the network configuration is demonstrated by the spatial aliasing effect which may distort the obtained spectra. This effect is similar to the one observed in the case of under-sampling of time series. Without the knowledge of the actual minimum characteristic wavelength of the field, there is no satisfactory way from multipoint measurements alone to identify whether spatial aliasing is occurring or not. Fortunately, in our case, additional spatial information about the magnetic field is used from the a priori knowledge included during the wave field identification. The main effect of this additional information is to moderate to a large extent the limitation due to aliasing (see *Pinçon et al.* [2000] for further details).

[28] Considering a network configuration and a duration of mission suitable to derive a valuable set of $\mathbf{k}(\omega)$, all these uncertainties may be considered as resulting in a global uncertainty of 20% on the impedance determinations. The related uncertainties on the $\sigma(r)$ profiles depend on the inversion procedure. Simulations using the stochastic procedure proposed by *Grandis et al.* [1999] have been made with possible models of conductivity distribution in Mars. The results show that knowing the impedance within a precision of about 20% for frequencies ranging from 1 Hz to 10^{-5} Hz allows one to probe the electrical structure of Mars for depths ranging from a few kilometers to a few hundreds of kilometers, and even 1200 kilometers in the case of a cold Mars mantle [*Mocquet and Menvielle*, 2000].

3.2.3. Network Seismic Experiment

[29] A very broadband seismic network on a planet records three types of waves: both longitudinally and transversely polarized high-frequency body waves (P- and S-waves), low-frequency surface waves, and free oscillations. In the case of radial symmetry, the inversion of travel times as a function of distance, and the inversion of waveform data, provide values of P- and S-wave speeds ($v_P(r)$, and $v_S(r)$, respectively), and information on the location at depth of major seismic interfaces, such as the radius of the core-mantle boundary r_{CMB} or the radius of the crust-mantle boundary r_{crust}. Free oscillation data could also provide additional information on the density profile of the planet and could be detectable on Mars [*Lognonné et al.*, 1996].

[30] The determination of wave velocities and depths of interfaces from the arrival times of seismic body waves is a classical problem, which is extensively explained in seismological textbooks [e.g., *Aki and Richards*, 1980, chap. 12; *Bullen and Bolt*, 1987, chap. 7]. Using ray geometry, the observed arrival time t of a body wave (either P or S) generated at the surface, and recorded at the epicentral distance Δ after traveling through a stack of concentric spherical shells, is

$$t = p\Delta + 2\int_{r_p}^{a} \frac{1}{r}\left[\left(\frac{r}{v}\right)^2 - \left(\frac{r_p}{v_p}\right)^2\right]^{\frac{1}{2}} dr, \qquad (6)$$

where the ray parameter p, i.e., the derivative of the travel time with respect to distance, is constant along ray path, v stands either for P- or S-wave speed at radius r, and the subscript p indicates that values are evaluated at the deepest point of the ray.

[31] For a given set of observations $t(\Delta)$, the retrieval of $v(r)$ using equation (6) is a nonlinear inverse problem, which is traditionally addressed in two ways: either by linearized inversion techniques applied in steps [e.g., *Johnson and Gilbert*, 1972], or by nonlinear inversion methods. The latter method is preferred for sparse nonterrestrial data [*Khan et al.*, 2000; *Khan and Mosegaard*, 2002; *Lognonné et al.*, 2003] because it makes it possible to analyze uncertainties and nonuniqueness of the output models. In practice, the planetary models are subdivided in a number of shells of variable size. Each layer is characterized by its physical extent, and by a smooth polynomial variation of seismic wave speeds.

[32] At present time, a complete description of the elastic structure has only been achieved for the Earth, and PREM [*Dziewonski and Anderson*, 1981] is now extensively used in both seismological and geodynamical studies of our planet. The record of lunar seismological data by the Apollo missions (for a review, see *Lognonné and Mosser* [1993]) provided a more restricted, but still very valuable set of information on the seismic properties of the mantle, and on the crustal thickness of the Moon [e.g., *Toksöz et al.*, 1974; *Goins et al.*, 1981; *Nakamura*, 1983; *Khan et al.*, 2000; *Vinnik et al.*, 2001; *Khan and Mosegaard*, 2002; *Lognonné et al.*, 2003]. The values of PREM are determined with an error of the order of a few tenths of a percent. For the Moon, the spatial distribution of the hypocenters, the restricted aperture of the network, and the monochromatic nature of Apollo records did not allow for the detection of a possible core, but modern techniques of signal processing and stochastic inversion enabled *Lognonné et al.* [2003] to reevaluate seismic velocities inside the Lunar mantle with an a posteriori error in the range 2–6%. This low uncertainty was obtained by a reprocessing of the whole data set produced between 1969 and 1977, including artificial impacts, meteorite impacts, shallow moonquakes, and deep tidally triggered moonquakes. A particular attention was devoted to the estimation of P and S arrival time errors, to the relocation of the events, and to a reassessment of the crustal thickness using converted phases at the crust-mantle boundary. The mean error of the arrival times used in the inversion was about 2 s. The variability of the 1-D model derived by *Lognonné et al.* [2003] is up to twice larger than the error on seismic velocity measurements. This result suggests lateral velocity variations which still need to be identified. A 2 s error is at least twice the worst expected error on the picking of body-wave arrival times using modern very broadband seismometers. Taking into account both the high-quality of the seismometers which are currently constructed for future planetary network missions [*Lognonné et al.*, 2000], and the moderate level of seismicity which is expected for Mars [*Phillips*, 1991; *Esposito et al.*, 1992; *Golombek et al.*, 1992], it can be reasonably expected that seismic velocity profiles of the Martian mantle will be determined with an error lower or equal to 2%. For a detailed statistical analysis of a seismic network efficiency on Mars, we refer the reader to *Mocquet* [1999].

[33] In the present study, the constraint provided by seismological data is defined by the acoustic wave speed v_ϕ:

$$v_\phi(r) = \sqrt{\phi(r)} = \sqrt{v_P^2(r) - \frac{4}{3}v_S^2(r)} = \sqrt{\frac{K(r)}{\rho(r)}}, \qquad (7)$$

where K is the bulk modulus, and ρ is the density. Two main reasons lead us to use $v_\phi(r)$ instead of P- and S-wave speeds separately. From the point of view of laboratory experiments, the pressure and temperature dependence of elastic moduli is by far better documented for bulk moduli than for shear moduli. Reviews concerning this topic are given by, e.g., *Duffy and Anderson* [1989], *Jackson and Rigden* [1998], *Vacher et al.* [1998], and *Jackson* [2000]. Moreover, the extrapolation of the results obtained in the laboratory at high frequencies (MHz to GHz) to the seismic frequency domain ($\sim$1 Hz), is also more difficult for the shear modulus than for the bulk modulus [e.g., *Karato*, 1993], because the dissipation of shear strain energy is about one

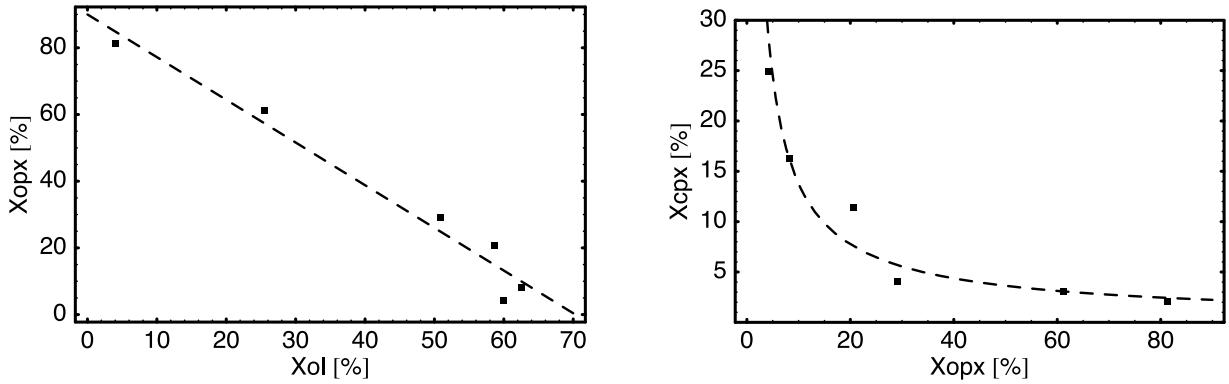

Figure 1. Relationships (left) between the volume contents of orthopyroxene X_{opx} and olivine X_{ol} and (right) between the volume contents of clinopyroxene X_{cpx} and X_{opx} in the terrestrial and Martian mineralogical models listed in Table 3. Dashed curves correspond to equations (8) and (9).

hundred times larger than the dissipation associated with volume changes. Promising data have been obtained by *Jackson et al.* [2002] on olivine polycrystals at high temperature and seismic frequencies, but the available data set is still not sufficiently documented for our purpose.

3.3. Parameters

[34] The crust is described by its mean thickness h_{crust} and its mean density ρ_{crust}. The parameters characterizing the core are its mass M_C and its radius r_{CMB}. The crustal thickness h_{crust} can be constrained by topographic, gravimetric and seismic data. Both the geodetic and seismic experiments constrain the values of r_{CMB}. The mantle composition is defined by the bulk fraction of iron x_{Fe}, and olivine fraction X_{ol}, where x and X refer to chemical and mineralogical fractions, respectively. For the sake of simplicity, and in view of the moderate size of Mars, the pressure profile is assumed to increase linearly with depth in the mantle [*Sohl and Spohn*, 1997; *Mocquet and Menvielle*, 2000], and the value of the pressure gradient dP/dr is a model parameter. The latter assumption of a linear increase of mantle pressure is not restrictive. It can be easily relaxed if a larger planet is considered.

3.4. Constraints From Laboratory Experiments

[35] The relations between the data and the parameters depend on mineralogical and thermodynamical constraints, which are provided by laboratory experiments. In this section, we present the relevant information to calculate the mineralogy of our Martian mantle models. We consider 11 different minerals or phases. Under the assumption of mantle chemical homogeneity, the mineralogical composition is uniquely defined at all depths, once the mantle parameters x_{Fe}, X_{ol}, dP/dr, and $T(r)$ are chosen. Experimental results on the phase diagrams of mantle minerals will be essential for this. The computation of observables entering our forward problem at standard temperature and pressure is explained below.

3.4.1. Starting Composition

[36] Once an olivine content X_{ol} is chosen, we calculate the composition of the non olivine subsystem. Let us consider previously published bulk compositions of the Earth [see, e.g., *Irifune*, 1987; *Javoy*, 1995] and Martian mantle [*Morgan and Anders*, 1979; *Dreibus and Wänke*, 1985; *Kamaya et al.*, 1993; *Bertka and Fei*, 1997; *Sanloup et al.*, 1999]. These compositions are listed in Table 3. Figure 1 plots the contents of orthopyroxenes (X_{opx}) versus olivine (X_{ol}) and clinopyroxenes (X_{cpx}) versus X_{opx}. The most striking relationship is the decrease of the volume fraction of (Mg, Fe)SiO_3 orthopyroxenes with increasing volume fraction of (Mg, Fe)$_2SiO_4$ olivine. The latter feature was indeed expected since both minerals are made of similar oxides. The second plot (Figure 1 (right)) enables us to define the relative proportions of ortho- and clinopyroxenes. The following empirical relations are proposed, assuming linear $X_{opx} - X_{ol}$ and power law $X_{cpx} - X_{opx}$ trends:

$$X_{opx} = -1.28X_{ol} + 90, \tag{8}$$

$$X_{cpx} = 92.3\left(X_{opx}\right)^{-0.837}, \tag{9}$$

$$X_{gt} = 100 - X_{ol} - X_{opx} - X_{cpx}, \tag{10}$$

where X_{gt} is the garnet content. For any chosen value of X_{ol}, these relations give a modal composition that is roughly consistent with the petrological or cosmochemical arguments classically used to model mantle bulk compositions, as listed in Table 3. Note that the proposed model precludes compositions made of more than 70.3 volume % olivine (see dashed line in Figure 1).

[37] The models of the Martian mantle reported in Table 3 all have Mg number (Mg #) in the range 70–80%. To broaden the set of mineralogies studied in this paper, we shall consider that the bulk iron fraction x_{Fe}, equal to (1 − Mg #), belongs to the range 10–40% [see also *Mocquet et al.*, 1996].

3.4.2. Phase Diagrams

[38] With the temperature and pressure increase, olivine, orthopyroxene, clinopyroxene and garnet undergo phase transitions. The volume fractions of the new mineral phases are computed using phase diagrams evaluated from laboratory measurements. Two independent subsystems are considered: the phase diagram of olivine and its high pressure phases, and a phase diagram for all other components.

[39] The phase diagram of olivine can be computed at any temperature, using calorimetric data. We use here the method and data of *Akaogi et al.* [1989]. We refer the

Table 3. Compositions Proposed for the Earth's and Mars' Mantle

	Earth		Mars			
	Pyrolite[a]	Primitive Mantle[b] (PM)	Morgan-Anders-Kamaya[c]	SNC Meteorites[d] (DW)	EH45-H55[e] (EH45)	EH70-H30[e] (EH70)
			Bulk Composition (wt %) in Major Oxides			
SiO_2	44.5	45.7	41.60	44.40	47.50	51.00
TiO_2	0.22	-	0.30	0.14	0.10	0.10
Al_2O_3	4.31	4.02	6.40	3.02	2.50	2.50
FeO	8.36	7.57	15.80	17.90	17.70	11.40
MnO	-	-	-	0.46	0.40	0.40
MgO	37.97	38.48	29.80	30.20	27.30	27.30
CaO	3.5	3.25	5.20	2.45	2.00	2.00
Na_2O	0.39	-	0.10	0.50	1.20	1.30
P_2O_5	0.44	-	-	0.16	-	-
Cr_20_3	-	-	0.60	0.76	0.70	0.60
Mg#	88	91	77	75	72	80
			Mineralogical Modes (vol %)			
Olivine	62.5	50.9	60	58.7	25.5	4.1
Orthopyroxenes	8.2	29.1	4.1	20.6	61.2	81.4
Clinopyroxenes	16.3	4.1	24.9	11.4	3.1	2.1
Garnets	13	15.9	10.9	9.3	10.2	12.4

[a]*Irifune* [1987].
[b]*Javoy* [1995], *Sanloup et al.* [1999].
[c]*Morgan and Anders* [1979], *Kamaya et al.* [1993].
[d]*Dreibus and Wänke* [1985], *Bertka and Fei* [1997].
[e]*Sanloup et al.* [1999].

reader to this paper for more details. The iron partitioning between perovskite and Mg-Wüstite is taken from *Andrault* [2001].

[40] The phase diagram of the other components, pyroxenes, garnet and their high pressure phases, is much more complex, and cannot be simply computed from calorimetric data. At pressures below 10 GPa (Figure 2), experimental results indicate that (Mg, Fe)SiO_3 pyroxenes exhibit several phase transitions (see *Ulmer and Stalder* [2001] for a recent review). At high temperatures and moderate pressures, Ca-poor pyroxene is orthorhombic (opx). A monoclinic polymorph is stable at low pressure and low temperature, LCpx, and another monoclinic polymorph forms at high pressure, HCpx. Experiments performed with fayalite-MgO-quartz mixtures at 1473 *K* constrain the width of the loop for the opx-HCpx transition to be at most 0.2 GPa [*Woodland*, 1998]. In the Earth's mantle, this phase transition might be the cause of the "X-discontinuity", occasionally reported at a depth of about 300 km [e.g., *Revenaugh and Jordan*, 1991; *Deuss and Woodhouse*, 2002]. Lower pressures in the Martian mantle will shift this phase transition to deeper depths.

[41] Consider now transformations of pyroxenes at higher pressures. A large number of experimental studies have been performed in the system $MgSiO_3$ (enstatite)-$Mg_3Al_2Si_3O_{12}$ (pyrope), because this system is probably the most relevant for studying the Earth's mantle, given its relatively high Al_2O_3 content and high Mg number. Indeed, if the olivine part of pyrolite is subtracted out, the bulk Al_2O_3 content in pyroxene and garnet must be around 12% [e.g., *Kubo and Akaogi*, 2000]. With such a composition, pyroxene dissolves into majoritic garnet at pressures around 14–16 GPa, both at low temperatures (i.e., 1273 K [*Kanzaki*, 1987]) and high temperatures (i.e., 1573, 1873 K [*Akaogi et al.*, 1987]). Then majorite is the stable phase with increasing pressures, up to the appearance of perovskite at about 22 GPa and 2023 or 2223 K [*Akaogi and Ito*, 1999]. Above 22 GPa, at lower temperatures, however, majorite first takes the akimotoite structure, and transforms into perovskite [e.g., *Irifune et al.*, 1996; *Kubo and Akaogi*, 2000; *Akaogi et al.*, 2002]. Figure 2 shows these different transformations in the pressure-temperature space.

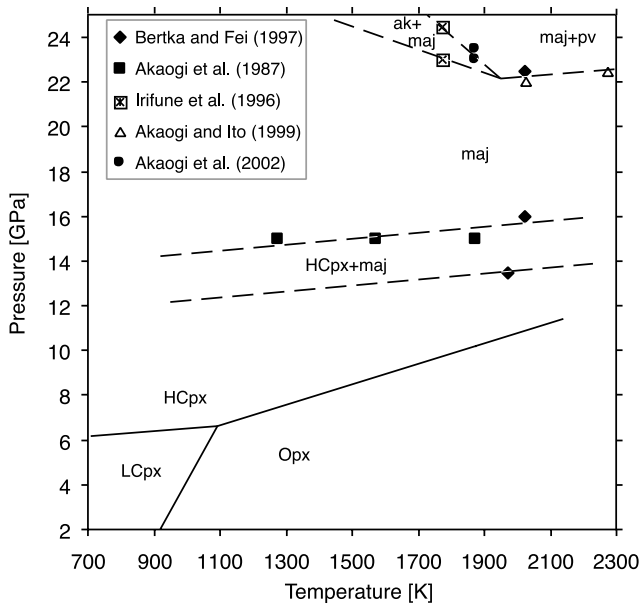

Figure 2. Phase diagram of pyroxenes and garnets. Solid [*Ulmer and Stalder*, 2001] and dashed curves correspond to well-determined and less constrained boundaries, respectively. The positions of these boundaries are discussed in the text. The letters ak, maj, pv, HCpx, LCpx, and Opx represent akimotoite, majorite, perovskite, high-pressure clinopyroxenes, and low-pressure clinopyroxenes and orthopyroxenes, respectively.

[42] Complexities may arise when considering bulk compositions of the Martian mantle. When compared to the Earth's mantle (see Table 3), the Martian mantle is probably iron rich (low Mg number) and Al_2O_3 depleted (except for the composition proposed by *Morgan and Anders* [1979]). These two features should stabilize an assemblage of ringwoodite + stishovite instead of majorite in the $MgSiO_3$-$FeSiO_3$ system at high temperature (i.e., 2023 K [*Ohtani et al.*, 1991]) and in the system $FeSiO_3$-$Fe_3Al_2Si_3O_{12}$ at low temperature (i.e., 1273 K [*Akaogi and Akimoto*, 1977]). However, we have chosen to consider only majorite in the phase diagram of Figure 2, for two main reasons. First, the experimental results mentioned above have been obtained for simple binary systems, but the combined effects of high Fe and low Al contents on pyroxene-garnets transitions is unknown. Second, the experiments of *Bertka and Fei* [1997] reported only majorite garnet (plus olivine high-pressure phases) in the pressure range 16–22 GPa, but no other phase.

[43] Finally, the question of Ca-bearing phases must be examined. At low pressures, Ca-pyroxene (diopside) is stable, and garnet contains a slight amount of CaO, that can be simulated as independent grossular for simplicity [e.g., *Vacher et al.*, 1998]. However, *Bertka and Fei* [1997] showed in their experiments that less than 5% Ca-garnet should form in a SNC composition. Furthermore, elastic properties of Ca-bearing garnet are relatively close to those of pyrope (see, e.g., compressional data of *Conrad et al.* [1999]), and electrical properties are still unknown, to our best knowledge. Therefore this mineral is neglected here. At high pressures, majorite is the only Ca-bearing phase reported in the experiments of *Bertka and Fei* [1997], who did not observe Ca-perovskite. This latter phase is therefore not included in the present study.

3.4.3. Experimental Data at Standard Temperature and Pressure

[44] For each mineral i we give here the constants appearing in the constitutive relations between the data and the parameters. The experimental values at Standard Temperature and Pressure (STP: $P_0 = 10^5$ Pa, $T_0 = 298$ K) are listed in Tables 1 and 2. We denote STP values by the subscript 0, unless stated otherwise.

[45] Table 1 lists the STP values of the constants needed to compute electrical conductivity. Further explanations are needed here. With some rare exceptions, electrical conduction is a thermally activated process and is well represented by an Arrhenius-type law,

$$\sigma^{(i)}(T,P) = \sigma_0^{(i)} e^{\frac{-\left(E_0^{(i)} + P\Delta V^{(i)}\right)}{kT}}, \tag{11}$$

where $E_0^{(i)}$ and $\sigma_0^{(i)}$ are the activation energy and the preexponential factor, respectively, $\Delta V^{(i)}$ is an activation volume, and k is Boltzmann's constant. In the case of materials which are expected to be present in the mantle of terrestrial planets, the activation volume is generally found to be very small, if not of the order of the experimental uncertainty, thus indicating a weak dependence on pressure of the electrical conductivity [e.g., *Duba et al.*, 1974; *Parkhomenko*, 1982; *Xu et al.*, 1998]. As a result of this, the pressure dependence is often disregarded, and so do we in the following.

[46] The preexponential factor $\sigma_0^{(i)}$ and the activation energy $E_0^{(i)}$ depend on the iron fraction in mineral i. This iron fraction $y^{(i)}$ is equal for all minerals to the bulk iron fraction x_{Fe} except at phase transitions where it is evaluated from phase diagrams.

[47] Equation (11) thus becomes

$$\sigma^{(i)}\left(T, y^{(i)}\right) = \sigma_0^{(i)}\left(y^{(i)}\right) e^{-\frac{E_0^{(i)}\left(y^{(i)}\right)}{kT}}. \tag{12}$$

[48] As we allow the bulk iron fraction to vary in the interval [10%, 40%], we need to know the iron dependence of the electrical conductivity. To our best knowledge, laboratory results that are available in the literature do not sample such a wide ($y^{(i)}$) domain for all minerals. We therefore estimate $\sigma^{(i)}$ ($y^{(i)}$) by means of empirical models. P. Vacher and O. Verhoeven (Modelling the electrical conductivity of iron-rich minerals for planetary applications, submitted to *Planetary and Space Science*, 2004; hereinafter referred to as Vacher and Verhoeven, submitted manuscript, 2004) show that all the measurements of the electrical conductivity of the various minerals considered in this paper can be described in terms of a simple empirical model:

$$\log\left(\sigma_0^{(i)}\left(y^{(i)}\right)\right) = \log\left(\sigma_{0;\,ref}^{(i)}\right) + \alpha^{(i)} \log\left(\frac{y^{(i)}}{y_{\mathrm{ref}}}\right), \tag{13}$$

$$E_0^{(i)}\left(y^{(i)}\right) = E_{0;\,ref}^{(i)} + \beta^{(i)}.\left(y^{(i)} - y_{\mathrm{ref}}\right). \tag{14}$$

[49] In these equations, $\sigma_{0;\,ref}^{(i)}$ is the value of the electrical conductivity for the limiting case where the temperature goes to infinity, and where the iron fraction is equal to y_{ref} and $E_0^{(i)}$ is the activation energy for an iron fraction equal to y_{ref}. This reference iron fraction y_{ref} is set to 0.1, which is the iron fraction usually assumed for the terrestrial mantle. The term $\alpha^{(i)}$ $\log(y^{(i)}/y_{\mathrm{ref}})$ expresses that the electrical conductivity is proportional to the concentration of the charge carriers, itself proportional to some power $\alpha^{(i)}$ of the iron fraction [*Tyburczy and Fisler*, 1995]. For most of the minerals we consider, the activation energy $E_0^{(i)}$ does not show any significant iron fraction dependence. For some minerals, however, such a dependence is observed: it can be accounted for by means of a linear term $\beta^{(i)}.(y^{(i)} - y_{\mathrm{ref}})$. The values of the constants entering equations (13) and (14) can be found in Table 1 for each mineral. Further details on the derivation and computation of the empirical models are given by P. Vacher and O. Verhoeven (submitted manuscript, 2004).

[50] Table 2 gives the STP values of experimental data for density and elastic moduli. The density $\rho_0^{(i)}$ at STP temperature T_0 and pressure P_0, and its temperature dependence, $\alpha^{(i)}(P_0,T)$ are obtained from laboratory results. The increase of density due to the iron substitution in the mineral (i) at STP conditions is noted $\rho_{0,Fe}^{(i)}$ in Table 2. The density of the mineral (i) at STP conditions is therefore computed as $\rho_0^{(i)} + y^{(i)}.\rho_{0,Fe}^{(i)}$. For most minerals, the variation of the thermal expansivity $\alpha^{(i)}(P_0,T)$ is well described by an empirical polynomial law (see, e.g., the compilation by *Saxena and Shen* [1992]):

$$\alpha^{(i)}(P_0,T) = a_0{}^{(i)} + b_0{}^{(i)}T - c_0{}^{(i)}T^{-2} + d_0{}^{(i)}T^{-1}, \tag{15}$$

where the constants $a_0^{(i)}$, $b_0^{(i)}$ and $c_0^{(i)}$ can be read from Table 2, and the constants $d_0^{(i)}$ are equal to zero except for the akimotoite for which it is equal to -0.1808 [*Ita and Stixrude*, 1992].

[51] The acoustic wave speed $v_\phi(r)$ is equal to the square root of the ratio of the bulk modulus K over the density ρ (see equation (7)). We show in Appendix A that the computation of K requires the knowledge of the isentropic bulk modulus $K_{S_0}^{(i)}$ and of its temperature and pressure derivatives, $\left.\frac{\partial K_S^{(i)}}{\partial T}\right|_0$ and $\left.\frac{\partial K_S^{(i)}}{\partial P}\right|_0$, respectively. According to laboratory results, the iron dependence of the bulk modulus is assumed to be linear, leading to a bulk modulus equal to, at STP conditions, $K_{S_0}^{(i)} + y^{(i)}.K_{S_0,Fe}^{(i)}$, where $K_{S_0,Fe}^{(i)}$ is the derivative of K_{S_0} with respect to iron content.

[52] It should be noted that the effect of aluminous phases is not accounted for in the constants listed in Table 2. We estimated from experimental works that including Al in pyroxene or garnet increases by less than 3% their respective seismic velocities.

4. Forward Problem

[53] This section details the forward problem used to compute synthetic MNS data from given parameter values. A previous version of the code which computes seismic velocities for given pressure-temperature conditions and mineralogical compositions of the Earth's upper mantle has been tested against radial seismic models [*Dziewonski and Anderson*, 1981; *Kennett et al.*, 1995] by *Vacher et al.* [1998]. A similar forward problem has also been used by *Cammarano et al.* [2003] to compute synthetic seismic velocities for the Earth. The trade-offs between uncertainties on composition, temperature and laboratory measurements are discussed in the latter paper. Concerning the electrical conductivity, our formula (equation (12)) reduces to the formula of *Xu et al.* [2000] when dealing with terrestrial minerals. The schema of our forward problem is as follows:

[54] 1. Compute from X_{ol} and x_{Fe} the relative amounts of orthopyroxene (equation (8)), clinopyroxene (equation (9)) and garnet (equation (10)).

[55] 2. Use the phase diagrams described in section 3.4.2 along with the temperature profile $T(r)$ and pressure gradient dP/dr to compute the volume fractions $X_i(r)$ of the different mineral phases. Derive also the iron fraction $y^{(i)}(r)$ of each mineral (i) from the bulk iron fraction x_{Fe}.

[56] 3. For each mineral (i), correct STP values of the density $\rho_0^{(i)}$ and bulk modulus $K_{S_0}^{(i)}$ for the effect of iron content using iron fraction $y^{(i)}(r)$ (see section 3.4.3).

[57] 4. For each mineral (i), compute the electrical conductivity $\sigma^{(i)}(r)$ (equation (12)) as a function of $T(r)$ and its iron fraction $y^{(i)}(r)$.

[58] 5. Use a two steps procedure (isobaric heating followed by adiabatic compression) to calculate the density $\rho^{(i)}(r)$ (equations (A8)–(A9)) and $K^{(i)}(r)$ (equation (A10)) of each mineral (i) as a function of $T(r)$ and $P(r)$. This procedure starts from measurements of density and bulk modulus at STP conditions and is explained in Appendix A.

[59] 6. Compute the density $\rho(r)$ of the assemblage at depth r as the arithmetic mean of individual densities $\rho^{(i)}(r)$ weighted by their volume fraction $X^{(i)}$. Bulk modulus $K(r)$ and electrical conductivities $\sigma(r)$ are computed from the individual values, $K^{(i)}(r)$ and $\sigma^{(i)}(r)$ respectively, using the procedure of *Hashin and Shtrikman* [1962, 1963].

[60] 7. From the values of $\rho(r)$ and $K(r)$, compute the acoustic wave speed profile $v_\phi(r)$ using equation (7) and the mass and moment of inertia of the crust and the mantle using equations

$$M = M_C + 4\pi \int_{r_{\mathrm{CMB}}}^{r_{\mathrm{crust}}} \rho(r) r^2 dr + \frac{4\pi}{3}\rho_{\mathrm{crust}}\left(a^3 - r_{\mathrm{crust}}^3\right), \qquad (16)$$

$$I_{m,c} = \frac{8\pi}{3} \int_{r_{\mathrm{CMB}}}^{r_{\mathrm{crust}}} \rho(r) r^4 dr + \frac{8\pi}{15}\rho_{\mathrm{crust}}\left(a^5 - r_{\mathrm{crust}}^5\right), \qquad (17)$$

where $r_{\mathrm{crust}} = a - h_{\mathrm{crust}}$ and a is the radius of the spherical planet.

[61] This procedure has to be slightly modified when we consider the possibility of a partial melt region in the Martian mantle. The detection of this region is performed before step 1 by looking at the depth where the temperature profile $T(r)$ crosses the solidus of anhydrous peridotite of *Takahashi* [1990]. A particular degree of melting depends on the temperature and on the water content, because the latter controls the position of the solidus in the pressure-temperature space. The past and current water contents and partial melting of the Martian mantle are still a matter of debate. The available data come from geochemical studies of SNC meteorites of different ages. Nevertheless the later data is relevant for a discussion on the generation of the primary basaltic Martian crust (e.g., by crystallization of a global magma ocean) and it cannot be used directly to constrain the present-day water content and thermal state of the Martian mantle. Indeed SNC meteorites were ejected several hundreds of million years ago, after the end of any water recycling process inside Mars. Considering the absence of current plate tectonics and volcanic activities on Mars, we thus assume that the degree of partial melting, if any, cannot exceed a few percent on a global scale. For a given temperature, the degree of partial melting X_{melt} is assessed using the lever rule between the solidus and the liquidus [*Takahashi*, 1990]. Considering that the Martian mantle is almost dry, it can be reasonably assumed that both density and incompressibility are not affected by anelastic relaxation. In such a case, the geodetic and seismic data are not expected to detect partial melting in the mantle. On the contrary, the electrical conductivity is highly sensitive to the presence of conductive fluids (melted rocks and/or H_2O-rich fluids) because their conductivity σ_f (typically between 1 and 10 S m^{-1}) is very large compared to that of unmelted materials (e.g., typically between 10^{-4} and 10^{-2} S m^{-1} for dry olivine under terrestrial mantle conditions). The electrical conductivity of iron-rich melted samples is poorly known, and we simply take it to be 1000 times larger than that of solid rock as suggested by, e.g., *Roberts and Tyburczy* [1999] or *Waff and Weill* [1975]. When the fraction of conductive fluids X_{melt} is low (typically lower than 1% [see, e.g., *Tarits*, 1986, and references therein]), the melted phase does not make up a continuous conductive network through the resistive matrix of unmelted materials. In this case, the bulk electrical conductivity is computed using the above procedure. If the percentage is larger than 1%, the melted rocks make up a continuous network, and

the bulk electrical conductivity is computed using the Hashin-Shtrikman upper bound for a two-body assemblage [*Waff*, 1974]: the solid rock, with volume fraction $(1 - X_{melt})$ and electrical conductivity computed as stated above, and the molten part, with volume fraction X_{melt} and electrical conductivity equal to 1000 times the value of the conductivity of the solid rock.

5. Models of Mars' Interior

[62] For each set of values chosen for the parameters h_{crust}, ρ_{crust}, x_{Fe}, X_{ol}, dP/dr, $T(r)$, r_{CMB} and M_{C}, the procedure described in last section allows us to compute synthetic data M, $I_{m,c}$, $\sigma(r)$, and $v_{\phi}(r)$. Although most of these data are currently not constrained, values for the mass and global moment of inertia have already been obtained from previous spatial missions [*Lemoine et al.*, 2001; *Yoder et al.*, 2003]. Therefore any realistic model of Mars' interior has to fit these observables. Of course, these two constraints do not impose values for all parameters and, prior to any network science result, a large set of models is still possible. In the following, we have chosen to describe eight of them. They correspond to particular choices for the thermal profile $T(r)$ and the mineralogy of the mantle parameterized by x_{Fe} and X_{ol}.

5.1. Thermal Profiles

[63] We propose to consider for the thermal profile $T(r)$ a cold temperature profile T_c and a hot one T_h (Figure 3). They correspond to plausible end-members suggested by the present-day results of models designed for Mars thermal evolution [*Breuer and Spohn*, 2003].

[64] *Breuer and Spohn* [2003] investigate the influence of an early epoch of plate tectonics on the crust production and the possible generation of a magnetic field. Their models include the redistribution of radioactive elements associated with melting and the production of crust. One of their conclusions is that such an early stage of plate tectonics cannot reconcile both an early magnetic field and an acceptable history for crust production. Therefore we prefer to use a simple model assuming stagnant lid cooling through the whole history of the Martian mantle. Our T_c profile may be considered as the lower bound of their calculation results. Down to 450 km depth, profile (T_c) is characterized by a thermal gradient of 2.7 K/km (conductive lid). Between 450 and 550 km depth, this gradient is decreased to 2.3 K/km corresponding to the boundary between the conductive stagnant lid and the thermal boundary layer. At greater depth, the temperature increases adiabatically (0.12 K/km) down to the core-mantle boundary. Using the liquidus and solidus of anhydrous peridotite of *Takahashi* [1990], we observe that profile (T_c) is always colder than the solidus temperature profile. This is always the case for present-day results of *Breuer and Spohn* [2003]; whatever the viscosity law, an early plate tectonics event would even cool more efficiently the mantle.

[65] However, more recent work by D. Breuer (personal communication, 2003) tends to indicate that a more realistic value of the thermal conductivity of crustal rocks may steepen the present-day temperature gradient in the lithosphere. The model associated with profile (T_h) proposes a value of 2 $\mathrm{W.m^{-1}.K^{-1}}$ for the thermal conductivity in the crustal basaltic layer, smaller than the mantle value (4 $\mathrm{W.m^{-1}.K^{-1}}$) used everywhere for the cold profile T_c. The value of the crustal thickness is 100 km. The conductive lid in profile T_h is $\sim$150 km thinner than in T_c. The temperature increases in three steps with three distinct gradients: 6.4 K/km and 3.4 K/km within the crust and the conductive mantle, respectively, followed by an adiabatic increase of 0.12 K/km down to the core-mantle boundary.

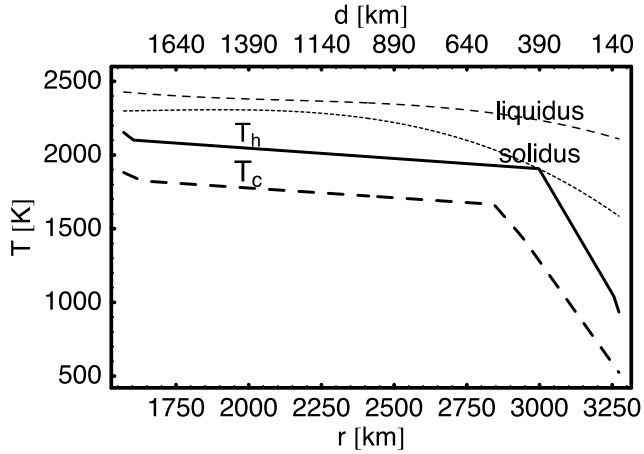

Figure 3. Temperature profiles for the mantle as functions of the radius r or depth d. The labels T_h and T_c refer to the hot and cold profiles, respectively. These two profiles may be considered as the end-members of the thermal evolution models of *Breuer and Spohn* [2003]. Solidus and liquidus are from *Takahashi* [1990]. The hot profile T_h induces a partial melt fraction of 1.8% at a depth of about 400 km.

[66] The change in thermal conductivity induces a thin layer of partial melt at a depth of about 400 km in profile (T_h) (Figure 3).

5.2. Compositions

[67] For each of the thermal profiles T_c and T_h (section 5.1), we consider four mantle compositions among those described in Table 3: (1) an Earth-like Primitive Mantle (PM) derived from *Javoy*'s [1995] geochemical composition, (2) the mineralogical (DW) model of *Bertka and Fei* [1997] derived from *Dreibus and Wänke*'s [1985] study of SNC meteorites, and (3 and 4) the two models proposed by *Sanloup et al.* [1999], where the Martian mantle composition is considered as a mixture of H and EH chondrites, namely, EH45 and EH70, where the number denotes the weight fraction of EH chondrites entering the Martian mantle composition.

[68] As can be observed from Figure 1, these four compositions are defined by olivine and bulk iron fractions which are very different from each other. Therefore the four compositions associated with the two extreme thermal profiles T_c and T_h lead to a sampling of our models of the internal structure of Mars.

5.3. Synthetic MNS Data Set

[69] For the eight models presented here, we divided the mantle into 100 layers of identical thickness (roughly 20 km).

[70] To specify a model, the mean crustal density ρ_{crust} and thickness h_{crust}, the pressure gradient in the mantle

Table 4. Models of the Martian Internal Structure Proposed to Simulate MNS Data Set[a]

	Model							
	PM_c	DW_c	$EH45_c$	$EH70_c$	PM_h	DW_h	$EH45_h$	$EH70_h$
h_{crust}, km	100	100	100	100	100	100	100	100
dP/dr, GPa/km	−0.012	−0.012	−0.012	−0.012	−0.012	−0.012	−0.012	−0.012
Temperature profile	T_c	T_c	T_c	T_c	T_h	T_h	T_h	T_h
x_{Fe}	0.09	0.25	0.28	0.2	0.09	0.25	0.28	0.2
X_{ol}	0.51	0.59	0.26	0.04	0.51	0.59	0.26	0.04
r_{CMB}, km	1800	1570	1570	1850	1900	1600	1600	1850
ρ_{crust}, kg m^{-3}	3199	2496	2549	2879	3203	2753	2814	3091
M_C, 10^{23} kg	1.606	1.136	1.143	1.657	1.847	1.201	1.207	1.688

[a]PM and DW refer to the mineralogical compositions derived from *Javoy* [1995] and *Dreibus and Wänke* [1985], respectively. EH45 and EH70 refer to the models proposed by *Sanloup et al.* [1999]. The index c or h refers to the thermal profile T_c or T_h, respectively. The Marstherm T_c is taken from *Breuer and Spohn* [2003]. The Marstherm T_h (D. Breuer, personal communication, 2003) allows for 1.8% of partial melting at a depth close to 400 km. ρ_{crust}, mean crustal density; x_{Fe}, bulk iron fraction of the mantle; X_{ol}, volume fraction of olivine in the mantle; dP/dr, pressure gradient; h_{crust}, crust thickness; M_C, core mass.

dP/dr, the core radius r_{CMB} and mass M_C remain to be set. In our layered model of the Martian mantle, both temperature profiles correspond to $h_{crust} \sim 100$ km. Accordingly the latter value is used for the 8 models. Values of ρ_{crust}, r_{CMB} and M_C are tuned in such a way that the mass of the whole planet is close to the measured value 6.41850 10^{23} kg [*Lemoine et al.*, 2001] and that the moment-of-inertia factor C/MR^2 is close to the value of 0.3650 obtained by *Yoder et al.* [2003]. Since the discretization of the problem induces numerical biases and since we consider an homogeneous core, we allow for uncertainties on the computed values of the total mass and C/MR^2 of 0.1% and 0.5%, respectively. Previous studies [*Mocquet et al.*, 1996; *Sohl and Spohn*, 1997] have shown that the value of the pressure gradient in the mantle is close to 0.012 GPa/km, and that it does not deviate by more than 0.1 MPa/km among previously published models. This value is therefore used here. The values of the parameters obtained for each model are listed in Table 4. In the following, the eight models are denoted by their mineralogies with an index c or h referring to the thermal profile T_c or T_h, respectively. The density is always greater for the cold mantle, resulting in lighter crust and core, as can be observed in Table 4.

[71] The synthetic mass of Mars M, the moment-of-inertia factor C/MR^2 and the moment of inertia of the mantle and crust $I_{m,c}$ are written in Table 5 for each model. The EH70 and PM mantles are so light that large values of the core size and crustal density are needed to get close to the C/MR^2 accepted range. Note that the model PM_h associated with a crust thickness of 100 km appears to be inconsistent with the mass and C/MR^2 constraints. Moreover, core radii larger than 1800 km seem too large regarding the results of *Yoder et al.* [2003]. As expected, models EH45 and DW lead to computed mass and C/MR^2 values closer to the observed values than PM and EH70. The simulated density, acoustic wave speed and electrical conductivity profiles are represented in panels a to c of Figures 4, 5, 6, and 7 for the DW, EH45, EH70 and PM models, respectively. The phase diagrams are computed following the procedure described in section 3.4.2. The mineralogical compositions of each model are represented on panels d and e of Figures 4, 5, 6, and 7 for the DW, EH45, EH70, and PM models, respectively. Note that perovskite and Mg-wüstite are not present in any model because the pressure at the core-mantle boundary is too small.

[72] The electrical conductivity of all the models corresponding to the hot profile T_h, denoted σ_h on the graphs, presents a peak of one order of magnitude at a depth close to 400 km. This is due to the presence of a very small region of partial melting in the upper mantle. The precise width and amplitude of this peak depend on both the chosen conductivity of the melted phase (chosen here to be 1000 times the conductivity of the solid rock; see section 4) and on the discretization of the mantle (here 100 layers of equal thickness). The mean $\log(\sigma)$ value averaged over the whole mantle appears slightly correlated with the bulk iron fraction: this value is roughly equal to −1.5 (for σ_h) and −2.5 (for σ_c) for both the PM and EH70 models (x_{Fe} = 0.09 and 0.2, respectively) and −0.5 (for σ_h) and −1.5 (for σ_c) for both DW and EH45 (x_{Fe} = 0.25 and 0.28, respectively).

[73] For all the models, the different zones of the temperature profiles are clearly recognizable on the simulated data. The shallow thermal conductive layer is marked by a stagnation or even a decrease of the density, a stagnation or a slight increase of the acoustic wave speed value and a several order of magnitude increase of the electrical conductivity. Down to the core mantle boundary, in the deeper convective region, the prevailing adiabatic conditions translate in a monotonic increase with depth of $v_\phi(r)$ and ρ, locally perturbed by the successive mineralogical transformations; the electrical conductivity variations are steplike. Between the occurrences of mineralogical transformations, the small temperature increase along the adiabats (less than 200 K across the whole layer) do not induce significant σ variations, here assumed to be pressure independent.

[74] Jumps corresponding to successive phase transitions (panels d and e of Figures 4, 5, 6, and 7) are clearly visible on the data profiles. For the DW and PM models (Figures 4 and 7), the jump corresponding to the olivine to wadsleyite transition can be observed in ρ, v_ϕ and σ at a depth of about 1000 km for DW and 1200 km for PM; for the EH45 and EH70 models (Figures 5 and 6), the v_ϕ profiles do not exhibit any significant sharp increase and the ρ profiles present a noticeable jump at a shallower depth of about 800–900 km, corresponding to the orthopyroxene to high pressure clinopyroxene transition. Note that the amplitude of the jumps in the ρ profile is larger for the EH70 model than for EH45. The variations in depth and amplitude of all these jumps are related to the three following parameters of

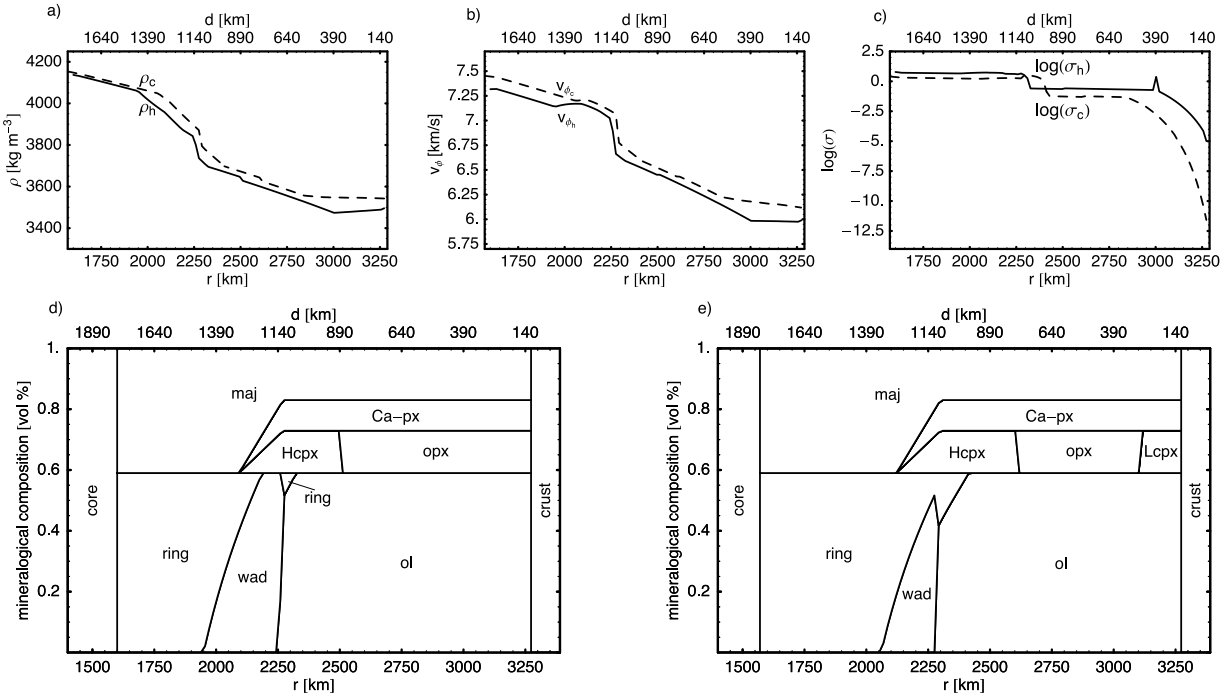

Figure 4. Synthetic data sets for the DW model. Figures 4a to 4c represent density ρ, acoustic wave speed v_ϕ, and logarithm of electrical conductivity log(σ) as a function of the radius r (lower scale) or depth d (upper scale). The solid and dashed curves correspond to the hot and cold temperature profiles, respectively. Note the conductivity spike induced by partial melting at a depth of 400 km for the hot Marstherm. Figures 4d and 4e represent mineralogical compositions (volume fractions) as a function of radius r or depth d for the hot and cold Marstherms, respectively. The letters ol, wad, ring, opx, Lcpx, Hcpx, Ca-px, and maj represent olivine, wadselyite, ringwoodite, orthopyroxene, low-pressure clinopyroxene, high-pressure clinopyroxene, Ca-pyroxene, and majorite, respectively.

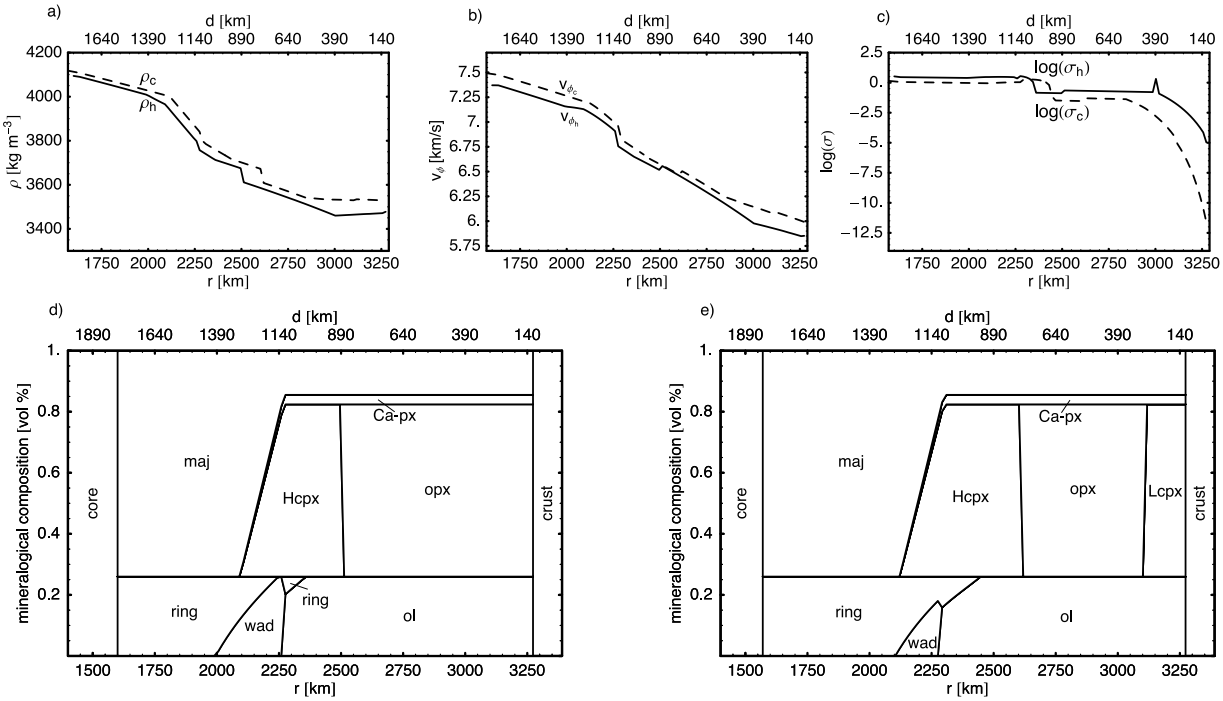

Figure 5. Synthetic data sets for the EH45 model. See Figure 4 for legend.

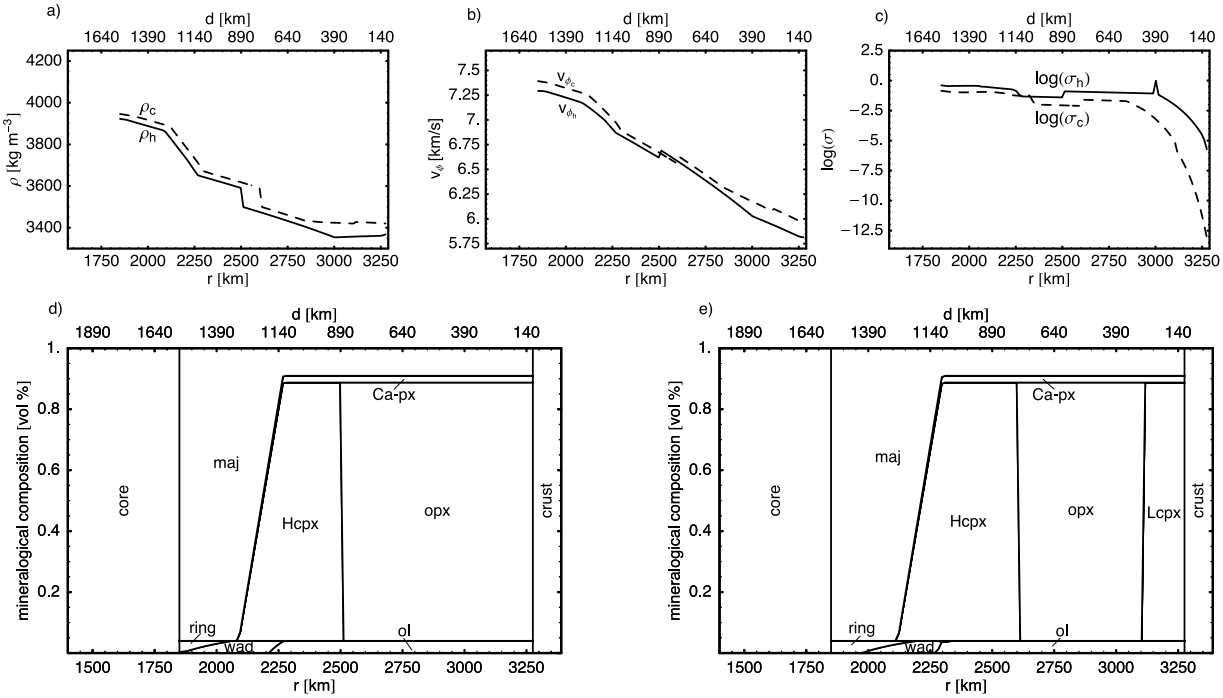

Figure 6. Synthetic data sets for the EH70 model. See Figure 4 for legend.

the models: X_{ol}, x_{Fe} and the temperature profile. The intersection of the thermal profile with various phase boundaries defines the depth of the corresponding jumps. The amplitude of a given jump results from the abundance of the phase undergoing the transition, related to X_{ol} through equations (8) to (10). Phase diagrams depend on the bulk iron fraction x_{Fe}; hence both depths and amplitudes of the jumps vary accordingly.

[75] The joint set of electromagnetic, geodetic and seismological data makes it possible to discriminate among the eight models. Down to 500 km depth, electromagnetic data are the most sensitive to temperature variations. In the deeper mantle, the value of the acoustic wave speed parameter v_Φ strongly depends on the mineralogical content. Concerning the bulk iron fraction of the mantle, electromagnetic data should enable us to discriminate among end-members

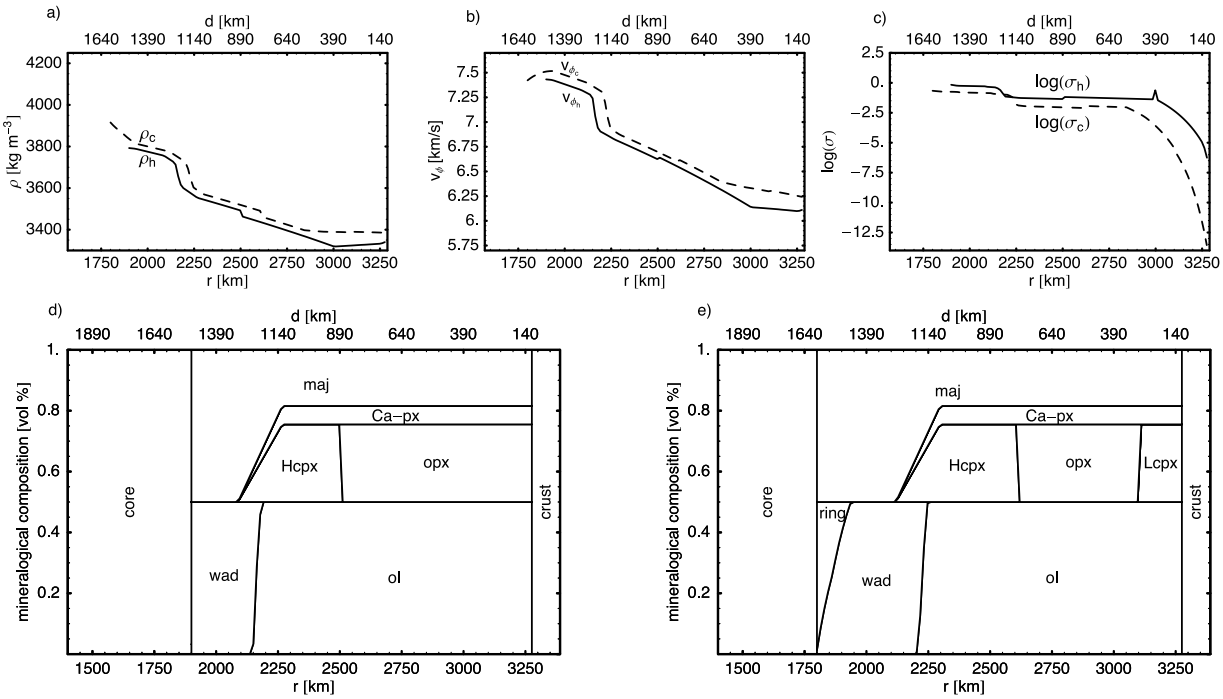

Figure 7. Synthetic data sets for the PM model. See Figure 4 for legend.

Table 5. Computed Global Observables for the 8 Models of the Martian Internal Structure[a]

	Model							
	PM_c	DW_c	$EH45_c$	$EH70_c$	PM_h	DW_h	$EH45_h$	$EH70_h$
M (10^{23} kg)	6.4249	6.4185	6.4185	6.4249	6.4442	6.4192	6.4185	6.4249
C/MR^2	0.3628	0.3632	0.3632	0.3628	0.3607	0.3632	0.3632	0.3621
$I_{m,c}$ (10^{36} kg m^2)	2.4610	2.5571	2.5565	2.4423	2.3944	2.5461	2.5455	2.4327

[a]For each model, M, C/MR^2, and $I_{m,c}$ represent the mass of Mars, the moment-of-inertia factor, and the moment of inertia of the mantle and crust, respectively, using our 100 layer model.

models, namely, an Earth-like mantle ($x_{Fe} \sim 0.1$) and an iron rich mantle ($x_{Fe} \sim 0.3$). The nonunique interpretation of conductivity increase, due to either temperature increase or iron enrichment, is expected to be resolved using geodetic and seismological data. A temperature increase results in a decrease of the density and a decrease of the acoustic wave speed while an iron enrichment in the mantle leads to an increase of the density and a decrease of v_ϕ. The possibility of discriminating between the different models with incomplete data will be addressed when considering the inversion (A. Rivoldini et al., manuscript in preparation, 2005).

6. Conclusion

[76] The procedure developed here emerged from a cooperation between members from geophysical teams of the NetLander project, which was devoted to network science on Mars. This planet is henceforth taken as an example of application, but the method is quite generic and can be applied with minor modifications to the study of any other telluric planet. The originality of the approach comes from the diversity of the geophysical data set, which derives from four different kinds of equations: equations derived from a potential for the geodetic data, diffusion equations for the electromagnetic data, propagation equations for the seismic waves, and constitutive and PVT equations for the physical properties of mantle minerals. In this first paper, we develop a method to construct physical and mineralogical models of the Martian mantle, suitable to be used in a future inversion of network data. Among this set, we choose eight mineralogical and physically sounded models which will be further used to assess the validity of the inverse method. Indeed the various models were chosen in order to test the resolving power of the complementary MNS data sets: on one hand, can we distinguish among several possible mineralogies (e.g., olivine- versus pyroxene-rich mantle) and thermal conditions? On the other hand, what are the parameters that the method can best resolve? These questions will be addressed in a companion paper (A. Rivoldini et al., manuscript in preparation, 2005).

Appendix A: PVT Equations of State for a Single Mineral

[77] In this appendix, we describe the method used to compute the density and bulk modulus of any mineral (i) at pressure $P(r)$ and temperature $T(r)$ from their respective laboratory measurements at STP conditions. Among proposed theories (see, e.g., *Jackson*'s [1998] review), we choose a two step procedure schematized in Figure A1. Assuming reversible elastic processes, we consider an isobaric heating of the mineral at pressure P_0, from T_0 to $\vartheta^{(i)}$ (A to B$^{(i)}$ paths in Figure A1), followed by an adiabatic compression from P_0, $\vartheta^{(i)}$ (points B$^{(i)}$) to P, T conditions (point C). Along the theoretical path AB$^{(i)}$C, $\vartheta^{(i)}$ is found as the temperature at P_0 along an adiabatic decompression (C to B$^{(i)}$ paths).

[78] Our modeling scheme is different from the one used in previous works where seismic velocities were computed from mineral physics. Usually, the temperature $\vartheta^{(i)}$ is determined by a trial and error method based upon a comparison between computed and observed density and seismic velocity profiles. These profiles are computed along an adiabatic path starting at $\vartheta^{(i)}$, P_0. The final temperature is a posteriori estimated [e.g., *Duffy and Anderson*, 1989; *Ita and Stixrude*, 1992; *Vacher et al.*, 1998; *Trampert et al.*, 2001]. In the present case, the final temperature to be reached at point C is known, and we have to find the value of $\vartheta^{(i)}$ at points B$^{(i)}$ in Figure A1 leading to the correct B$^{(i)}$C adiabatic path. Such an approach makes it necessary to compute simultaneously

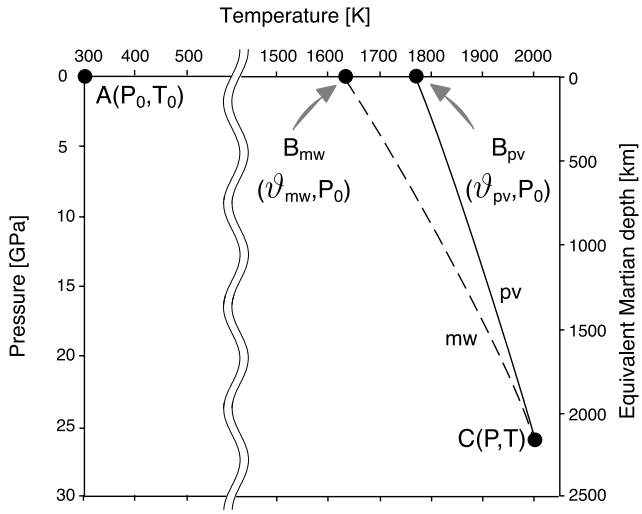

Figure A1. Thermodynamical paths, discussed in Appendix A, linking standard pressure and temperature (point A) to local pressure and temperature (point C). For each mineral (i), we consider an isobaric heating from point A to point B$^{(i)}$ followed by an adiabatic compression to point C. The temperature $\vartheta^{(i)}$, corresponding to the point B$^{(i)}$, is different for each mineral. It is defined as the temperature at standard pressure such that an adiabatic compression would lead the mineral (i) to the local pressure and temperature conditions of point C. Two examples are drawn: the solid curve is for the perovskite (pv), and the dashed one is for the Mg-Wüstite (mw).

the values of $\vartheta^{(i)}$, $\rho^{(i)}$ and $K_S^{(i)}$. This computation requires trial-error iterations for each mineral (i) taken separately.

[79] Figure A1 illustrates how different the $\vartheta^{(i)}$ values may be from one mineral to another. Let us suppose that we want to compute the values of the density and of the seismic velocities of perovskite and magnesiowüstite at a depth of 2200 km inside Mars, and at a temperature of 2000 K. This temperature value is reached at 2200 km depth for temperatures $\vartheta^{(i)}$ equal to 1770 K and 1630 K, for perovskite and magnesiowüstite, respectively. Our procedure assures, as illustrated in Figure A1, that all considered minerals are at the same temperature at a given depth, which is a necessary condition to get a relevant model of a mantle in thermodynamical equilibrium. Note that the latter procedure enables one to compute the local values of K (r) in equation (7) using the isentropic values $K_S^{(i)}(r)$ of each mineral i, where the subscript S indicates constant entropy, even though the actual temperature profile is not necessarily adiabatic.

[80] For the sake of simplicity, the mineral index (i) is omitted in the following subsections and in Figure A1.

A1. Definition of the Temperature ϑ

[81] The temperature variation along an adiabatic compression path is described by the thermodynamic Grüneisen's parameter γ_{th} [e.g., *Poirier*, 2000]:

$$\gamma_{th} = \left(\frac{\partial \ln T}{\partial \ln \rho}\right)_S. \tag{A1}$$

The value of Grüneisen's parameter is mainly a function of pressure and, to a lesser extent, of the temperature. Following the results of laboratory experiments [*Anderson*, 1979], we choose to use the quasiharmonic assumption

$$\gamma_{th}(P,T)\rho(P,T)^q = \text{constant}, \tag{A2}$$

where q is a constant usually equal to 1. Integrating equation (A1) at constant entropy and using (A2), we obtain

$$T = \vartheta e^{\frac{\gamma_{th_0}}{q}\left[\frac{\rho_0}{\rho(P_0,\vartheta)}\right]^q\left[1-\left(\frac{\rho(P_0,\vartheta)}{\rho(P,T)}\right)^q\right]}. \tag{A3}$$

The latter equation allows us to evaluate, from P and T values, and for each mineral taken separately, the temperature ϑ using a trial and error procedure.

A2. Isobaric Heating From A to B

[82] In order to evaluate the density ρ (P_0, ϑ) in equation (A3), we start from the definition of the thermal expansivity α,

$$\left(\frac{\partial \rho}{\partial T}\right)_{P_0} = -\alpha(P_0,T)\,\rho(P_0,T). \tag{A4}$$

Using the polynomial development (15), and integrating equation (A4) at constant pressure P_0, we obtain for each mineral

$$\rho(P_0,\vartheta) = \rho_0\left(\frac{T_0}{\vartheta}\right)^{d_0} \cdot \exp\left[a_0(T_0-\vartheta) + \frac{b_0}{2}\left(T_0^2-\vartheta^2\right) + c_0\left(\frac{1}{T_0}-\frac{1}{\vartheta}\right)\right]. \tag{A5}$$

The value of the adiabatic bulk modulus $K_S(P_0, \vartheta)$ is computed at constant P_0 using the formula

$$K_S(P_0,\vartheta) = K_{S0}\left(\frac{\rho(P_0,\vartheta)}{\rho_0}\right)^{\delta_{S_0}}, \tag{A6}$$

where δ_{S_0} is the Anderson-Grüneisen parameter, defined by

$$\delta_{S_0} = -\frac{1}{\alpha_0}\left(\frac{\partial \ln K_S}{\partial T}\right)_{P_0}. \tag{A7}$$

The value of the Anderson-Grüneisen parameter can be reasonably considered as independent of the temperature [*Anderson*, 1988]. It is thus only computed at STP conditions for each mineral.

A3. Adiabatic Compression From B to C

[83] The value of the local density $\rho(P(r), T(r))$ is obtained by computing the unique negative real root of the fourth order equation of state

$$P(r) = -(1-2\varepsilon)^{5/2}\left(C_1\varepsilon + \frac{1}{2}C_2\varepsilon^2 + \frac{1}{6}C_3\varepsilon^3\right), \tag{A8}$$

where

$$\varepsilon = \frac{1}{2}\left\{1 - \left[\frac{\rho(P,T)}{\rho(P_0,\vartheta)}\right]^{2/3}\right\} \tag{A9}$$

is the Eulerian strain of the mineral under adiabatic compression. The coefficients of the expansion (A8) are defined by the values of the bulk modulus and of its first and second derivatives with respect to pressure [e.g., *Davies and Dziewonski*, 1975]. Writing

$$K_S(r) = (1-2\varepsilon)^{5/2}\left(L_1 + L_2\varepsilon + \frac{1}{2}L_3\varepsilon^2\right) \tag{A10}$$

and considering the definition of K_S, the coefficients entering the expansions (A8) and (A10) are related through

$$\begin{cases} C_1 = 3\,L_1 \\ C_2 = 3\,L_2 + 7\,C_1 \\ C_3 = 3\,L_3 + 9\,C_2. \end{cases} \tag{A11}$$

Taking the limits at zero strain of equation (A10), and of its first and second derivatives with respect to pressure, yields [e.g., *Jackson*, 1998; *Trampert et al.*, 2001]

$$L_1 = K_S \tag{A12}$$

$$L_2 = K_S\left[5 - 3\left(\frac{\partial K_S}{\partial P}\right)\right] \tag{A13}$$

$$L_3 = K_S\left\{9\,K_S\frac{\partial^2 K_S}{\partial^2 P} + \left[5 - 3\left(\frac{\partial K_S}{\partial P}\right)\right]\left[7 - 3\left(\frac{\partial K_S}{\partial P}\right)\right]\right\} \tag{A14}$$

and

$$C_1 = 3\,K_S \tag{A15}$$

$$C_2 = 9\,K_S\left[4 - \left(\frac{\partial K_S}{\partial P}\right)\right] \tag{A16}$$

$$C_3 = 27\,K_S\left\{K_S\frac{\partial^2 K_S}{\partial^2 P} - \left(\frac{\partial K_S}{\partial P}\right)\left[7 - \left(\frac{\partial K_S}{\partial P}\right)\right] + \frac{143}{9}\right\}. \tag{A17}$$

[84] In equations (A12) to (A17), all quantities are evaluated at (P_0, ϑ) conditions. Since the second mixed derivative $\frac{\partial^2 K_S}{\partial T \partial P}$ is poorly constrained by laboratory measurements, we assume that $\frac{\partial K_S}{\partial P}$ is temperature independent at ambient pressure, namely,

$$\left(\frac{\partial K_S}{\partial P}\right)_{(P_0,\vartheta)} \approx \left(\frac{\partial K_S}{\partial P}\right)_{(P_0,T_0)}. \quad \text{(A18)}$$

[85] *Jackson* [1998] showed that the approximation (A18) is valid for the bulk modulus. The second derivative of K_S with respect to pressure has only been measured with large uncertainties for a very small number of minerals, namely, olivine [*Zha et al.*, 1998], magnesiowüstite [*Sinogeikin and Bass*, 2000], and orthopyroxene [*Flesch et al.*, 1998]. Following *Trampert et al.* [2001], we estimate its theoretical value by truncating the Birch-Murnaghan equation of state (A8) to third-order in strain, which means that the value of C_3 is set equal to zero in equation (A17). The validity of the latter approximations has been discussed in the previously cited studies of the Earth's lower mantle. Their validity is strengthened for the Martian mantle, because the pressure value which is reached at Mars' CMB (~23–25 GPa) is equal to the pressure value at the top of the Earth's lower mantle.

[86] **Acknowledgments.** This work benefited from the support of the European Community's Improving Human Potential Programme under contract RTN2-2001-00414, MAGE. It has also benefited from the support of the French Space Agency (CNES) to the MagNet, Neige, and Seis experiments in the frame of the preparation of the Netlander mission. Two of us (A.R. and O.V.) are acknowledging the support of the Belgian Science Policy Office (PRODEX). O.V. acknowledges a postdoctoral fellowship in Laboratoire de Planétologie et Géodynamique, Nantes, provided by the MAGE European Community Programme. The research of A.R. was supported by Belgian Federal Science Policy Office Action 2. We thank D. Breuer for useful discussions and sending us her results of thermal models prior to publication. We also thank F. Nimmo, T. Spohn, and an anonymous reviewer for valuable comments on the manuscript.

References

Acuña, M. H., et al. (1999), Global distribution of crustal magnetization discovered by the Mars Global surveyor MAG/ER experiment, *Science*, *284*, 790–793.

Akaogi, M., and S. Akimoto (1977), Pyroxene-garnet solid solution equilibria in the system $Mg_4Si_4O_{12}$-$Mg_3Al_2Si_3O_{12}$ and $Fe_4Si_4O_{12}$-$Fe_3Al_2Si_3O_{12}$ at high pressures and temperatures, *Phys. Earth Planet. Inter.*, *15*, 90–106.

Akaogi, M., and E. Ito (1999), Calorimetric study on majorite-perovskite transition in the system $Mg_4Si_4O_{12}$-$Mg_3Al_2Si_3O_{12}$: Transition boundaries with positive pressure-temperature slopes, *Phys. Earth Planet. Inter.*, *114*, 129–140.

Akaogi, M., A. Navrotsky, T. Yagi, and S. Akimoto (1987), Pyroxene-garnet transformation: Thermochemistry and elasticity of garnet solid solutions, and application to a pyrolite mantle, in *High-Pressure Research in Mineral Physics*, *Geophys. Monogr. Ser.*, vol. 39, edited by M. H. Manghani and Y. Syono, pp. 251–260, AGU, Washington, D. C.

Akaogi, M., E. Ito, and A. Navrotsky (1989), Olivine-modified spinel-spinel transitions in the system Mg_2SiO_4-Fe_2SiO_4: Calorimetric measurements, thermochemical calculation, and geophysical application, *J. Geophys. Res.*, *94*, 15,671–15,685.

Akaogi, M., A. Tanaka, and E. Ito (2002), Garnet-ilmenite perovskite transitions in the system $Mg_4Si_4O_{12}$-$Mg_3Al_2Si_3O_{12}$ at high pressures and high temperatures: Phase equilibria, calorimetry and implications for mantle structure, *Phys. Earth Planet. Inter.*, *132*, 303–324.

Aki, K., and P. G. Richards (1980), *Quantitative Seismology*, vols. 1 and 2, W. H. Freeman, New York.

Anderson, D. L. (1988), Temperature and pressure derivatives of elastic constants with application to the mantle, *J. Geophys. Res.*, *93*, 4688–4700.

Anderson, O. L. (1979), Evidence supporting the approximation $\gamma\rho$ = const for the Grüneisen parameter of the Earth lower mantle, *J. Geophys. Res.*, *84*, 3537–3542.

Andrault, D. (2001), Evaluation of (Mg, Fe) partitioning between silicate perovskite and magnesiowüstite up to 120 GPa and 2300 K, *J. Geophys. Res.*, *106*, 2079–2087.

Angel, R. J., and D. A. Hugh-Jones (1994), Equations of state and thermodynamic properties of enstatite pyroxene, *J. Geophys. Res.*, *99*, 19,777–19,783.

Barriot, J. P., et al. (2001), NEIGE: NetLander Ionosphere and Geodesy Experiment, *Adv. Space Res.*, *28*, 1237–1249.

Berdichevsky, M. N., E. B. Fainberg, N. M. Rotanova, J. B. Smirnov, and L. L. Vanyan (1976), Deep electromagnetic investigations, *Ann. Geophys.*, *32*, 143–155.

Bertka, C. M., and Y. Fei (1997), Mineralogy of the Martian interior up to core-mantle boundary pressures, *J. Geophys. Res.*, *102*, 5251–5264.

Bertka, C. M., and Y. Fei (1998), Density profile of an SNC model of Martian interior and the moment-of-inertia of Mars, *Earth Planet. Sci. Lett.*, *157*, 79–88.

Bills, B. G., and A. J. Ferrari (1978), Mars topography harmonics and geophysical implications, *J. Geophys. Res.*, *83*, 3497–3508.

Born, G. H. (1974), Mars physical parameters as determined from Mariner 9 observations of the natural satellites and Doppler tracking, *J. Geophys. Res.*, *79*, 4837–4844.

Breuer, D., and T. Spohn (2003), Early plate tectonics versus single-plate tectonics on Mars: Evidence from magnetic field history and crust evolution, *J. Geophys. Res.*, *108*(E7), 5072, doi:10.1029/2002JE001999.

Bullen, K. E., and B. A. Bolt (1987), *An Introduction to the Theory of Seismology*, 4th ed., 499 pp., Cambridge Univ. Press, New York.

Cammarano, F., S. Goes, P. Vacher, and D. Giardini (2003), Inferring upper mantle temperatures from seismic velocities, *Phys. Earth Planet. Inter.*, *138*, 197–222.

Conrad, P. G., C.-S. Zha, H.-K. Mao, and R. J. Hemley (1999), The high pressure, single crystal elasticity of pyrope, grossular, and andradite, *Am. Mineral.*, *84*, 374–383.

Davies, G. F., and A. M. Dziewonski (1975), Homogeneity and constitution of the Earth's lower mantle and outer core, *Phys. Earth Planet. Inter.*, *10*, 336–343.

Dehant, V., T. Van Hoolst, and P. Defraigne (2000), Comparison between the nutations of the planet Mars and the nutations of the Earth, *Surv. Geophys.*, *21*, 89–110.

Deuss, A., and J. H. Woodhouse (2002), A systematic search for mantle discontinuities using SS-precursors, *Geophys. Res. Lett.*, *29*(8), 1249, doi:10.1029/2002GL014768.

Dewaele, A., G. Fiquet, D. Andrault, and D. Hausermann (2000), P-V-T equation of state of periclase from synchrotron radiation measurements, *J. Geophys. Res.*, *105*, 2869–2877.

Dobson, D. P., and J. P. Brodholdt (2000), The electrical conductivity of the lower mantle phase magnesiowüstite at high temperatures and pressures, *J. Geophys. Res.*, *105*, 531–538.

Dreibus, G., and H. Wänke (1985), Mars, a volatile-rich planet, *Meteoritics*, *20*, 367–381.

Duba, A., H. C. Heard, and R. N. Schnock (1974), Electrical conductivity of olivine at high pressure and under controlled oxygen fugacity, *J. Geophys. Res.*, *79*, 1667–1673.

Duffy, T. S., and D. L. Anderson (1989), Seismic velocities in mantle minerals and the mineralogy of the upper mantle, *J. Geophys. Res.*, *94*, 1895–1912.

Dziewonski, A. M., and D. L. Anderson (1981), Preliminary reference Earth model, *Phys. Earth Planet. Inter.*, *25*, 297–356.

Esposito, P. B., W. B. Banerdt, G. F. Lindal, W. L. Sjogren, M. A. Slade, B. G. Bills, D. E. Smith, and G. Balmino (1992), Gravity and topography, in *Mars*, edited by H. H. Kieffer et al., pp. 209–248, Univ. of Ariz. Press, Tucson, Ariz.

Fiquet, G., D. Andrault, A. Dewaele, T. Charpin, M. Kunz, and D. Haüserman (1998), P-V-T equation of state of $MgSiO_3$ perovksite, *Phys. Earth Planet. Inter.*, *105*, 21–31.

Flesch, L. M., B. Li, and R. C. Liebermann (1998), Sound velocities of polycrystalline $MgSiO_3$ orthopyroxene to 10 GPa at room temperature, *Am. Mineral.*, *83*, 444–450.

Folkner, W. M., C. F. Yoder, D. N. Yuan, E. M. Standish, and R. A. Preston (1997), Interior structure and seasonal mass redistribution of Mars from radio tracking data of Mars Pathfinder, *Science*, *278*, 1749–1752.

Gapcynski, J. P., R. H. Tolson, and W. H. Michael Jr. (1977), Mars gravity field: Combined Viking and Mariner 9 results, *J. Geophys. Res.*, *82*, 4325–4327.

Goins, N. R., A. M. Dainty, and M. N. Toksöz (1981), Lunar seismology: The internal structure of the Moon, *J. Geophys. Res.*, *86*, 5061–5074.

Golombek, M. P., W. B. Banerdt, K. L. Tanaka, and D. M. Tralli (1992), A prediction of Mars seismicity from surface faulting, *Nature*, *258*, 979–981.

Grandis, H., M. Menvielle, and M. Roussignol (1999), Bayesian inversion with Markov Chains: 1. The 1-D magnetotelluric case, *Geophys. J. Int.*, *138*, 757–768.

Harri, A. M., et al. (1999), Network Science Landers for Mars, *Adv. Space Res.*, *23*, 1915–1924.

Hashin, Z., and S. Shtrikman (1962), A variational approach to the theory of the effective magnetic permeability of multiphase materials, *J. Appl. Phys.*, *33*, 3125–3131.

Hashin, Z., and S. Shtrikman (1963), A variational approach to the theory of the elastic behaviour of multiphase materials, *J. Mech. Phys. Solids*, *11*, 127–140.

Hinze, E., G. Will, and L. Cemic (1981), Eletrical conductivity measurements on synthetic olivines and on olivine enstatite and diopside from Dreiser Weiher, Eifel (Germany) under defined thermodynamic acivities as a function of temperature and pressure, *Phys. Earth Planet. Inter.*, *25*, 245–254.

Hjelt, S. E., and T. Korja (1993), Lithospheric and upper mantle structures: Results of electromagnetic soundings in Europe, *Phys. Earth Planet. Inter.*, *79*, 137–177.

Irifune, T. (1987), An experimental investigation of the pyroxene-garnet transformation in a pyrolite composition and its bearing on the constitution of the mantle, *Phys. Earth Planet. Inter.*, *45*, 324–336.

Irifune, T., T. Koizumi, and J.-I. Ando (1996), An experimental study of the garnet-perovskite transformation in the system $MgSiO_3$-$Mg_3Al_2Si_3O_{12}$, *Phys. Earth Planet. Inter.*, *96*, 147–157.

Ita, J., and L. Stixrude (1992), Petrology, elasticity, and composition of the mantle transition zone, *J. Geophys. Res.*, *97*, 6849–6866.

Jackson, I. (1998), Elasticity, composition and temperature of the Earth's lower mantle: A reappraisal, *Geophys. J. Int.*, *134*, 291–311.

Jackson, I. (2000), Laboratory measurement of seismic wave dispersion and attenuation: Recent progress, in *Earth's Deep Interior: Mineral Physics and Tomography From the Atomic to the Global Scale*, *Geophys. Monogr. Ser.*, vol. 117, edited by S. Karato et al., pp. 265–289, AGU, Washington, D. C.

Jackson, I., and S. M. Rigden (1988), Composition and temperature of the Earth's mantle: Seismological models interpreted through experimental studies of Earth materials, in *The Earth's Mantle, Composition, Structure, and Evolution*, edited by I. Jackson, pp. 405–460, Cambridge Univ. Press, New York.

Jackson, I., J. D. Fitz Gerald, U. H. Faul, and B. H. Tan (2002), Grain-size-sensitive seismic wave attenuation in polycrystalline olivine, *J. Geophys. Res.*, *107*(B12), 2360, doi:10.1029/2001JB001225.

Jackson, J. M., S. V. Sinogeigin, and J. D. Bass (1999), Elasticity of Mg SiO_3 orthoenstatite, *Am. Mineral.*, *84*, 677–680.

Jackson, J. M., S. V. Sinogeigin, and J. D. Bass (2000), Sound velocities and elastic properties of γ-Mg_2SiO_4 to 873 K by Brillouin spectroscopy, *Am. Mineral.*, *85*, 296–303.

Javoy, M. (1995), The integral enstatite chondrite model of the Earth, *Geophys. Res. Lett.*, *22*, 2219–2222.

Johnson, L. E., and F. Gilbert (1972), Inversion and inference for teleseismic ray data, in *Seismology: Body Waves and Sources*, *Methods in Comput. Phys.*, vol. 12, edited by B. A. Bolt, pp. 231–266, Elsevier, New York.

Kamaya, N., E. Ohtani, T. Kato, and K. Onuma (1993), High pressure phase transitions in a homogeneous model Martian mantle, in *Evolution of the Earth and Planets*, *Geophys. Monogr. Ser.*, vol. 74, edited by E. Takahashi, R. Jeanloz, and D. Rubie, pp. 19–26, AGU, Washington, D.C.

Kanzaki, M. (1987), Ultrahigh-pressure phase relations in the system $Mg_4Si_4O_{12}$-$Mg_3Al_2Si_3O_{12}$, *Phys. Earth Planet. Inter.*, *49*, 168–175.

Karato, S. (1993), Importance of anelasticity in the interpretation of seismic tomography, *Geophys. Res. Lett.*, *20*, 1623–1626.

Katsura, T., N. Mayama, K. Shouno, M. Sakai, A. Yoneda, and I. Suzuki (2001), Temperature derivatives of elastic moduli of $(Mg_{0.91}Fe_{0.09})_2SiO_4$ modified spinel, *Phys. Earth Planet. Inter.*, *124*, 163–166.

Kennett, B. L. N., E. R. Engdahl, and R. Buland (1995), Constraints on seismic velocities in the Earth from travel times, *Geophys. J. Int.*, *122*, 108–124.

Khan, A., and K. Mosegaard (2002), An inquiry into the lunar interior: A nonlinear inversion of the Apollo lunar seismic data, *J. Geophys. Res.*, *107*(E6), 5036, doi:10.1029/2001JE001658.

Khan, A., K. Mosegaard, and K. M. Rasmussen (2000), A new seismic velocity model for the Moon from a Monte Carlo inversion of the Apollo Lunar Seismic data, *Geophys. Res. Lett.*, *27*, 1591–1594.

Kieffer, H. H., B. M. Jakosky, C. W. Snyder, and M. S. Matthews (Eds.) (1992), *Mars*, 1498 pp., Univ. of Ariz. Press, Tucson.

Kubo, A., and M. Akaogi (2000), Post-garnet transitions in the system $Mg_4Si_4O_{12}$ - $Mg_3Al_2Si_3O_{12}$ up to 28 GPa: Phase relations of garnet, ilmenite and perovskite, *Phys. Earth Planet. Inter.*, *121*, 85–102.

Kuckes, A. F. (1973a), Relations between electrical conductivity of a mantle and fluctuating magnetic fields, *Geophys. J. R. Astron. Soc.*, *32*, 119–131.

Kuckes, A. F. (1973b), Correspondence between the magnetotelluric and field penetration depth analysis for measuring electrical conductivity, *Geophys. J. R. Astron. Soc.*, *32*, 381–385.

Kuhnke, F., M. Menvielle, G. Musmann, J.-F. Karczewski, H. Kügler, C. Cavoit, and P. Schibler (1998), Magnetic measurements onboard landers and related magnetic cleanliness program: The example of the OPTIMISM = MAG Mars-96 experiment, *Planet. Space. Sci.*, *46*, 749–767.

Langlais, B., M. E. Purucker, and M. Mandea (2004), Crustal magnetic field of Mars, *J. Geophys. Res.*, *109*, E02008, doi:10.1029/2003JE002048.

Lemoine, F. G., D. E. Smith, D. D. Rowlands, M. T. Zuber, G. A. Neumann, D. S. Chin, and D. E. Pavlis (2001), An improved solution of the gravity field of Mars (GMM-2B) from Mars Global Surveyor, *J. Geophys. Res.*, *106*, 23,359–23,376.

Li, B., and R. C. Liebermann (2000), Sound velocities of wadsleyite β-$(Mg_{0.88}Fe_{0.12})_2Si0_4$ to 10 Gpa, *Am. Mineral.*, *85*, 292–295.

Lognonné, P., and B. Mosser (1993), Planetary seismology, *Surv. Geophys.*, *14*, 239–302.

Lognonné, P., J. Gagnepain-Beyneix, W. B. Banerdt, S. Cacho, J. F. Karczewski, and M. Morand (1996), An ultra-broad band seismometer on InterMarsnet, *Planet. Space Sci.*, *44*, 1237–1249.

Lognonné, P., et al. (2000), The NetLander Very Broad Band Seismometer, *Planet. Space Sci.*, *48*, 1289–1302.

Lognonné, P., J. Gagnepain-Beyneix, and H. Chenet (2003), A new seismic model of the Moon: Implication for structure, thermal evolution and formation of the Moon, *Earth Planet. Sci. Lett.*, *211*, 27–44.

Longhi, J., E. Knittle, J. R. Holloway, and H. Wänke (1992), The bulk composition, mineralogy and internal structure of Mars, in *Mars*, edited by H. H. Kieffer et al., pp. 184–208, Univ. of Ariz. Press, Tucson.

McSween, H. Y., Jr. (1985), SNC meteorites: Clues to Martian petrologic evolution?, *Rev. Geophys.*, *23*, 391–416.

Menvielle, M., F. Kuhnke, G. Musmann, B. Tsurutani, and J.-F. Karczewski (1996), Contribution of surface magnetic recordings to planetary exploration, *Planet. Space Sci.*, *44*, 1289–1302.

Menvielle, M., et al. (2000), Contribution of magnetic measurements onboard NetLander to Mars exploration, *Planet. Space Sci.*, *48*, 1231–1247.

Mocquet, A. (1999), A search for the minimum number of stations needed for seismic networking on Mars, *Planet. Space Sci.*, *47*, 397–409.

Mocquet, A., and M. Menvielle (2000), Complementarity of seismological and electromagnetic sounding methods for constraining the structure of the Martian mantle, *Planet. Space Sci.*, *48*, 1249–1260.

Mocquet, A., P. Vacher, O. Grasset, and C. Sotin (1996), Theoretical seismic models of Mars: The importance of the iron content of the mantle, *Planet. Space Sci.*, *44*, 1251–1268.

Morgan, J. W., and E. Anders (1979), Chemical composition of Mars, *Geochim. Cosmochim. Acta*, *43*, 1601–1610.

Motschmann, U., T. I. Woodward, K. H. Glassmeier, D. J. Southwood, and J. L. Pinçon (1996), Wavelength and direction filtering by magnetic measurements at satellite arrays: Generalized minimum variance analysis, *J. Geophys. Res.*, *101*, 4961–4965.

Nakamura, Y. (1983), Seismic velocity structure of the lunar mantle, *J. Geophys. Res.*, *88*, 677–686.

Ohtani, E., N. Kagawa, and K. Fujino (1991), Stability of majorite (Mg, Fe)SiO_3 at high pressures and 1800°C, *Earth Planet. Sci. Lett.*, *102*, 158–166.

Parker, R. L., and K. A. Whaler (1981), Numerical methods for establishing solutions to the inverse problem of electromagnetic induction, *J. Geophys. Res.*, *86*, 9574–9584.

Parkhomenko, E. I. (1982), Electrical resistivity of minerals and rocks at high temperature and pressure, *Rev. Geophys.*, *20*, 193–218.

Parkinson, W. D., and V. R. S. Hutton (1989), The electrical conductivity of the Earth, in *Geomagnetism*, vol. 3, edited by J. A. Jacobs, pp. 261–321, Elsevier, New York.

Phillips, R. J. (1991), Expected rate of Marsquake: Scientific rationale and requirements for a global seismic network on Mars, *LPI Tech. Rep. 91-02*, pp. 35–38, Lunar and Planet. Inst., Houston, Tex.

Pinçon, J. L., and F. Lefeuvre (1991), Local characterization of homogeneous turbulence in a space plasma from simultaneous measurements of field components at several points in space, *J. Geophys. Res.*, *96*, 1789–1802.

Pinçon, J. L., and F. Lefeuvre (1992), The application of the generalized Capon method to the analysis of a turbulent field in space plasma: Experimental constraints, *J. Atmos. Terr. Phys.*, *54*, 1237–1247.

Pinçon, J. L., M. Menvielle, and L. Szarka (2000), Geomagnetic induction study using the Netlander network of magnetometers, *Planet. Space Sci.*, *48*, 1261–1270.

Poirier, J. P. (2000), *Introduction to the Physics of the Earth's Interior*, 2nd ed., 264 pp., Cambridge Univ. Press, New York.

Poirier, J.-P., and J. Peyronneau (1992), Experimental determination of the electrical conductivity of the material of the Earth's lower mantle, in *High-Pressure Research: Application to Earth and Planetary Sciences*, *Geophys. Monogr. Ser.*, vol. 39, edited by Y. Syono and M. H. Manghnani, pp. 77–87, AGU, Washington, D. C.

Revenaugh, J., and T. H. Jordan (1991), Mantle layering from ScS reverberations: 3. The upper mantle, *J. Geophys. Res.*, *96*, 19,781–19,810.

Reynard, B., and D. C. Rubie (1996), High pressure, high temperature Raman spectroscopic study of ilmenite-type $MgSiO_3$, *Am. Mineral.*, *81*, 1092–1096.

Roberts, J. J., and J. A. Tyburczy (1999), Partial-melt electrical conductivity: Influence of melt composition, *J. Geophys. Res.*, *104*, 7055–7065.

Sanloup, C., A. Jambon, and P. Gillet (1999), A simple chondritic model of Mars, *Phys. Earth Planet. Inter.*, *112*, 43–54.

Saxena, S. K., and G. Shen (1992), Assessed data on heat capacity, thermal expansion, and compressibility for some oxides and silicates, *J. Geophys. Res.*, *97*, 19,813–19,825.

Schmucker, U. (1970), Anomalies of geomagnetic variations in the southwestern United States, *Bull. Scripps Inst. Oceanogr.*, *13*, 1–165.

Seifert, K. F., G. Will, and R. Voigt (1982), Electrical conductivity measurements on synthetic pyroxenes $MgSiO_3$ - $FeSiO_3$ at high pressures and temperatures under defined thermodynamic conditions, in *High Pressure Researches in Geoscience*, edited by W. Schreyer, pp. 419–432, E. Schweizerbart, Stuttgart, Germany.

Shankland, T. J., J. Peyronneau, and J.-P. Poirier (1993), Electrical conductivity of the Earth's lower mantle, *Nature*, *366*, 453–455.

Sinogeikin, S. V., and J. D. Bass (2000), Single crystal elasticity of pyrope and MgO to 20 GPa by Brillouin scattering in the diamond cell, *Phys. Earth Planet. Inter.*, *120*, 43–62.

Sinogeikin, S. V., and J. D. Bass (2002), Elasticity of Majorite and a Majorite-Pyrope solid solution to high pressure: Implications for the Transition Zone, *Geophys. Res. Lett.*, *29*(2), 1017, doi:10.1029/2001GL013937.

Sinogeikin, S. V., T. Katsura, and J. D. Bass (1998), Sound velocities and elastic properties of Fe-bearing wadsleyite and ringwoodite, *J. Geophys. Res.*, *103*, 20,819–20,825.

Sinogeikin, S. V., J. D. Bass, and T. Katsura (2001), Single-crystal elasticity of γ- $(Mg_{0.91}\ Fe_{0.09})_2\ Si0_4$ to high pressures and to high temperatures, *Geophys. Res. Lett.*, *28*, 4335–4338.

Sohl, F., and T. Spohn (1997), The interior structure of Mars: Implications from SNC meteorites, *J. Geophys. Res.*, *102*, 1613–1635.

Spohn, T., F. Sohl, and D. Breuer (1998), Mars, *Astron. Astrophys. Rev.*, *8*, 181–236.

Takahashi, E. (1990), Speculations on the Archean mantle: Missing link between komatiite and depleted garnet peridotite, *J. Geophys. Res.*, *95*, 15,941–15,954.

Tarits, P. (1986), Conductivity and fluids in the oceanic upper mantle, *Phys. Earth Planet. Inter.*, *42*, 215–226.

Tarits, P., and V. Jouanne (1990), Résultats de sondages magnétotelluriques sous-marins et structure thermique des points chauds, *Bull. Soc. Geol.*, 921–931.

Toksöz, M. N., A. M. Dainty, S. C. Solomon, and K. A. Anderson (1974), Structure of the Moon, *Rev. Geophys.*, *12*, 539–567.

Trampert, J., P. Vacher, and N. Vlaar (2001), Sensitivities of seismic velocities to temperature, pressure and composition in the lower mantle, *Phys. Earth Planet. Inter.*, *124*, 255–267.

Tyburczy, J. A., and D. K. Fisler (1995), Electrical properties of minerals and melts, in *Mineral Physics and Cristallography: A Handbook of Physical Constants*, *AGU Ref. Shelf*, vol. 2, edited by T. J. Ahrens, pp. 185–208, AGU, Washington, D. C.

Ulmer, P., and R. Stalder (2001), The Mg (Fe) Si O_3 orthoenstatite-clinoenstatite transitions at high pressures and temperatures determined by Raman-spectroscopy on quenched samples, *Am. Mineral.*, *86*, 1267–1274.

Vacher, P., A. Mocquet, and C. Sotin (1998), Computation of seismic profiles from mineral physics: The importance of the non-olivine components for explaining the 660 km depth discontinuity, *Phys. Earth Planet. Inter.*, *106*, 275–298.

Vinnik, L., H. Chenet, J. Gagnepain-Beyneix, and P. Lognonné (2001), First seismic receiver functions on the Moon, *Geophys. Res. Lett.*, *28*, 3031–3034.

Waff, H. S. (1974), Theoretical considerations of electrical conductivity in partially molten mantle and implications for geothermometry, *J. Geophys. Res.*, *79*(26), 4003–4010.

Waff, H. S., and D. F. Weill (1975), Electrical conductivity of magmatic liquids: Effects of temperature, oxygen fugacity and composition, *Earth Planet. Sci. Lett.*, *28*, 254–260.

Wang, Y., D. J. Weidner, J. Zhang, G. D. Gwanmesia, and R. C. Liebermann (1998), Thermal equation of state of garnets along the pyrope-majorite join, *Phys. Earth Planet. Inter.*, *105*, 59–71.

Wang, Z., and S. Ji (2001), Elasticity of six polycristalline silicate garnets at pressure up to 3.0 Gpa, *Am. Mineral.*, *86*, 1209–1218.

Wieczorek, M. A., and M. T. Zuber (2004), Thickness of the Martian crust: Improved constraints from geoid-to-topography ratios, *J. Geophys. Res.*, *109*, E01009, doi:10.1029/2003JE002153.

Woodland, A. B. (1998), The orthorhombic to high-P monoclinic phase transition in Mg-Fe pyroxenes: Can it produce a seismic discontinuity?, *Geophys. Res. Lett.*, *25*, 1241–1244.

Woodland, A. B., and R. J. Angel (1997), Reversal of the orthoferrosilite-high-P clinoferrosilite transition, a phase diagram for $FeSiO_3$ and implications for the mineralogy of the Earth's upper mantle, *Eur. J. Mineral.*, *9*, 245–254.

Xu, Y., B. T. Poe, T. J. Shankland, and D. C. Rubie (1998), Electrical conductivity of olivine, wadsleyite, and ringwoodite under upper mantle conditions, *Science*, *280*, 1415–1418.

Xu, Y., T. J. Shankland, and B. T. Poe (2000), Laboratory-based electrical conductivity in the Earth's mantle, *J. Geophys. Res.*, *105*, 27,865–27,875.

Yoder, C. F., and E. M. Standish (1997), Martian precession and rotation from Viking lander range data, *J. Geophys. Res.*, *102*, 4065–4080.

Yoder, C. F., A. S. Konopliv, D. N. Yuan, E. M. Standish, and W. M. Folkner (2003), Fluid core size of Mars from detection of the solar tide, *Science*, *300*, 299–303.

Yseboodt, M., J. Barriot, and V. Dehant (2003), Analytical modeling of the Doppler tracking between a lander and a Mars orbiter in terms of rotational dynamics, *J. Geophys. Res.*, *108*(E7), 5076, doi:10.1029/2003JE002045.

Zha, C.-S., T. S. Duffy, R. T. Downs, H.-K. Mao, and R. J. Hemley (1998), Brillouin scattering and X-ray diffraction of San Carlos olivine: Direct pressure determination to 32 Gpa, *Earth Planet. Sci. Lett.*, *159*, 25–33.

Zhang, J., and P. Kostak Jr. (2002), Thermal equation of state of magnesiowüstite $(Mg_{0.6}\ Fe_{0.4})O$, *Phys. Earth Planet. Inter.*, *129*, 301–311.

Zhang, L., H. Ahsbahs, A. Kutoglu, and C. A. Geiger (1999), Single-crystal hydrostatic compression of synthetic pyrope, almandine, spessartine, grossular and andradite garnets at high pressures, *Phys. Chem. Miner.*, *27*, 52–58.

Zhao, Y., R. B. Von Dreele, J. Z. Zhang, and D. J. Weidner (1998), Thermoelastic equation of state of monoclinic pyroxene: $CaMgSi_2O_6$ diopside, *Rev. High Pressure Sci. Technol.*, *7*, 25–27.

Zuber, M. T., et al. (2000), Internal structure and early thermal evolution of Mars from Mars Global Surveyor topography and gravity, *Science*, *287*, 1788–1793.

J.-P. Barriot, Groupement de Recherche en Géodésie Spatiale, CNES, Toulouse, France. (jean-pierre.barriot@cnes.fr)

G. Choblet, A. Mocquet, P. Vacher, and O. Verhoeven, Laboratoire de Planétologie et Géodynamique, UMR-CNRS 6112, UFR des Sciences et des Techniques, 2, Rue de la Houssinière, BP 92 208, 44 322 Nantes Cedex 3, France. (gael.choblet@univ-nantes.fr; antoine.mocquet@univ-nantes.fr; pierre.vacher@univ-nantes.fr; olivier.verhoeven@univ-nantes.fr)

V. Dehant, A. Rivoldini, J. Sleewaegen, and T. Van Hoolst, Royal Observatory of Belgium, 3 Avenue Circulaire, 1180 Bruxelles, Belgium. (veronique.dehant@oma.be; rivoldini@oma.be; timvh@oma.be; olivier.verhoeven@oma.be)

P. Lognonné, Département de Géophysique Spatiale et Planétaire, UMR7096, Institut de Physique du Globe de Paris, Saint Maur des Fossés, France. (lognonne@ipgp.jussieu.fr)

M. Menvielle, CETP/IPSL, UMR CNRS/UBSQ 8639, Observatoire de Saint-Maur, Saint Maur des Fossés, France. (michel.menvielle@cetp.ipsl.fr)